

Quantum algorithms for compact polymer thermodynamics

Davide Rattacaso^{1,2}, Daniel Jaschke^{1,2,3,4}, Antonio Trovato^{1,2}, Ilaria Siloi^{1,2} and Simone Montangero^{1,2}

¹*Dipartimento di Fisica e Astronomia “G. Galilei” & Padua Quantum Technologies
Research Center, Università degli Studi di Padova, Italy I-35131, Padova, Italy*

²*INFN, Sezione di Padova, via Marzolo 8, I-35131, Padova*

³*PlanQC GmbH, Lichtenbergstr. 8, 85748 Garching, Germany*

⁴*Institute for Complex Quantum Systems, Ulm University, Albert-Einstein-Allee 11, 89069 Ulm, Germany*

(Dated: March 16, 2026)

Efficient sampling from ensembles of Hamiltonian cycles is critical for predicting the thermodynamic properties of compact polymers, with applications including modeling protein and RNA folding and designing soft materials. Although classical Monte Carlo methods are widely regarded as the standard approach, their efficiency is strongly limited when applied to compact polymers. In this work, we enable a quadratic speedup in the estimation of thermodynamic properties of maximally compact polymers and heteropolymers by quantum computation. To this end, we encode the target thermodynamic ensemble into the amplitudes of a quantum state, i.e., a quantum sample, which can be processed via amplitude amplification. Using quantum equational reasoning, we construct a local parent Hamiltonian whose unique ground state realizes a quantum sample of all Hamiltonian cycles. This state can be prepared on quantum hardware using ground-state preparation methods, such as quantum annealing, and subsequently manipulated to generate quantum samples of polymers and heteropolymers at a target temperature. Finally, we approximate the quantum sample as a tensor network, revealing an entanglement area law. For fixed-width rectangular lattices, we obtain a time-efficient and compact encoding of the full ensemble of Hamiltonian cycles, enabling the efficient evaluation of expectation values, partition functions, and configuration probabilities via tensor contractions, without resorting to sampling.

I. INTRODUCTION

Hamiltonian paths are curves on a lattice that visit each vertex exactly once. These paths serve as mathematical models for the spatial organization of compact polymers [1–5], such as globular proteins [6] and packaged viral RNA [7–9]. Understanding the statistical properties of the complete ensemble of such curves on a fixed lattice is essential for predicting their thermodynamic behavior.

Classical Monte Carlo (MC) methods are commonly employed to investigate polymer thermodynamics: sampling compact polymers poses significant challenges for MC [4, 10–12]. Transfer matrix methods [13, 14] provide an alternative to Monte Carlo sampling, but their applicability is restricted by the exponential increase in computational cost with the shorter dimensions of the two—or three—dimensional lattice

In recent years, quantum computation has emerged as a promising approach for efficiently simulating and predicting the physics of soft-matter systems described by lattice-path configurations [15–17]. The standard approach is to encode the spatial configurations of polymers in the degenerate ground states of a classical spin Hamiltonian [15, 16], which can be prepared by quantum annealing [18–21]. However, this encoding requires an exponentially increasing number of spins and pairwise interactions when applied to modeling compact polymers. This exponential overhead is intrinsic to the topological nature of the problem: the existence of one single Hamiltonian path connecting all lattice sites cannot be enforced by a collection of purely local Boolean constraints [22], that is, a collection of local classical spin interactions. As

shown in Ref. [17], a possible solution is to construct a lattice gauge model with compact polymer configurations as degenerate ground states.

In addition to the potential acceleration in preparing classical configurations via quantum processes such as quantum annealing, quantum computation provides a provable quadratic speedup for sampling expectation values and partition functions of statistical ensembles using amplitude amplification [23]. Achieving this speedup requires encoding the target probability distribution $p(\boldsymbol{\sigma})$ over the space of classical configuration $\boldsymbol{\sigma}$ into the amplitudes of a corresponding quantum state $|\psi\rangle = \sum_{\boldsymbol{\sigma}} \sqrt{p(\boldsymbol{\sigma})} |\boldsymbol{\sigma}\rangle$, referred to as a coherent quantum sample [24]. In this paper, we unlock this quantum advantage by departing from the standard quantum optimization paradigm, in which polymer configurations are encoded in the degenerate ground states of a classical Hamiltonian. Instead, we leverage equational reasoning [25] to construct a non-diagonal parent Hamiltonian \hat{H}_{HC} whose unique zero-energy ground state, $|X_{\text{HC}}\rangle$, is a coherent quantum sample of all compact polymer configurations. Remarkably, the parent Hamiltonian that we construct is local, meaning that both the number of interactions per monomer and their range do not scale with system size.

Numerous algorithms could be employed to prepare the state $|X_{\text{HC}}\rangle$. Examples include quantum annealing [18–21], optimal control techniques [26–28], quantum approximate optimization algorithms [29–31], and dissipative time-evolution methods [32–36]. The performance of these approaches depends on both the specific problem instance and the details of their implementation.

The construction the parent Hamiltonian \hat{H}_{HC} for $|X_{\text{HC}}\rangle$ is explained in Section II. To construct \hat{H}_{HC} , we define a set of local transformations between spin configurations that act as discrete homotopies, connecting all and only those configurations that represent topologically equivalent — i.e., containing the same number of disjoint closed paths with the same nesting structure — ensembles of loops on the lattice. Leveraging the recently introduced framework of quantum equational reasoning [25], from these transformations we build a local Hamiltonian whose ground space is an equal-amplitude superposition for each class of topologically equivalent configurations. We then introduce an additional local term that lifts the energy of all sectors corresponding to configurations with more than one loop, thereby restricting the ground-state subspace of the full parent Hamiltonian \hat{H}_{HC} to the single, coherent quantum sample $|X_{\text{HC}}\rangle$.

The state $|X_{\text{HC}}\rangle$ encodes an infinite temperature ensemble in which all configurations are assigned equal probability. In Section III, we show how imaginary time evolution [32–35] can transform this state into a coherent quantum sample corresponding to an arbitrary temperature Boltzmann distribution of polymers. The approach is further extended to the thermodynamics of heteropolymers, where the spatial arrangement of distinct monomers determines the energy of each configuration. To this end, we design a quantum circuit that dresses the vertices of each Hamiltonian path with a target sequence of monomers, thereby mapping the state $|X_{\text{HC}}\rangle$ to a coherent quantum sample of heteropolymer configurations.

Finally, in Section IV, we approximate the ground state of \hat{H}_{HC} as a matrix product state [37, 38], thereby establishing a quantum-inspired framework to generate a compressed representation of the entire ensemble of closed Hamiltonian paths. The resulting state obeys an area law for entanglement entropy, which enables an efficient matrix-product-state approximation when one lattice dimension is fixed. Under these conditions, tensor network contractions can be used to efficiently compute expectation values, determine the partition function, and evaluate the probability of arbitrary configurations without resorting to sampling.

II. CONSTRUCTION OF THE PARENT HAMILTONIAN

Here, we construct a local, frustration-free Hamiltonian \hat{H}_{HC} whose unique ground state $|X_{\text{HC}}\rangle$ is a coherent quantum sample encoding the complete set of closed Hamiltonian paths, named Hamiltonian cycles, on a rectangular lattice.

The construction relies on a set of local constraints that enforce the Hamiltonian condition, together with a family of local transformations that relate configurations that encode topologically equivalent paths. These ingredients naturally lead to a decomposition of the configuration space into topological sectors and allow us to analyze the

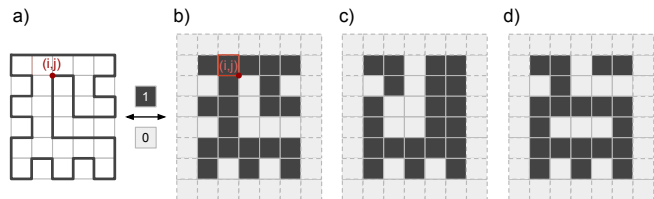


FIG. 1. *Hamiltonian cycles and multiloop configurations over lattices and dual lattices.* **Panel (a):** Hamiltonian cycle over a rectangular lattice. **Panel (b):** configuration of the dual lattice encoding the Hamiltonian cycle in Panel (a). **Panel (c):** configuration of the dual lattice encoding a multiloop violating the Hamiltonian condition: some vertex is never visited, and some vertex is visited two times. **Panel (d):** configuration of the dual lattice encoding a 2-factor violating the single-loop condition, as it consists of two disjoint loops.

spectral properties of \hat{H}_{HC} .

A. Hamiltonian cycles as binary configurations

As a first step, we map Hamiltonian cycles to configurations of a binary system. We only consider graphs that can be embedded on a two-dimensional surface. By the Jordan curve theorem [39], any closed path on such a graph separates the surface into two disjoint regions: an interior, namely the region enclosed by the path, and an exterior.

We now focus on the case of rectangular lattices with $n \times m$ vertices. A Hamiltonian cycle is a closed path that visits each vertex exactly once. To translate this notion into a binary representation, we introduce the *dual lattice*, whose sites correspond to the $(n - 1) \times (m - 1)$ plaquettes of the square lattice — namely, the elementary regions into which the embedding subdivides the surface. In this picture, a Hamiltonian cycle is uniquely specified by the set of plaquettes lying in its interior: the boundary between interior and exterior plaquettes traces exactly the closed path on the original lattice. This construction gives rise to a natural binary encoding: for each dual plaquette we assign the value 1 if it lies inside the cycle and 0 otherwise (see Fig. 1, Panels (a) and (b)).

For convenience, we extend the dual lattice by adding a fixed boundary frame of plaquettes in the state 0. This modification is not essential to the construction but simplifies the definition of the operators introduced below. Under this convention, the dual lattice contains $(n + 1) \times (m + 1)$ plaquettes, and each vertex (i, j) of the original lattice is surrounded by the four dual plaquettes $[[i, j), (i, j + 1)], [(i + 1, j), (i + 1, j + 1)]$ (see Fig. 1, Panels (a) and (b)).

Each Hamiltonian cycle corresponds to a binary configuration of the dual lattice. However, the converse does not hold: a generic dual configuration represents a *multiloop*, namely a collection of closed paths that may in-

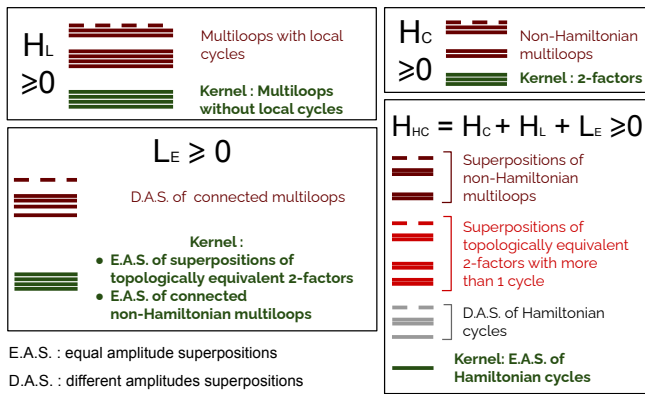


FIG. 2. *Schematic construction of the parent Hamiltonian \hat{H}_{HC} .* The Hamiltonian is expressed as the sum of three local positive semidefinite Hamiltonians, each enforcing a distinct condition on the states in its kernel. The ground state of \hat{H}_{HC} simultaneously lies in these three kernels.

intersect or overlap on the original lattice (see Fig. 1). To single out configurations corresponding to Hamiltonian cycles, two independent conditions must be met. The first is the *Hamiltonian condition*, which enforces only those configurations that visit every vertex of the lattice exactly once (see Fig. 1, Panel c for a counterexample). Such configurations form collections of disjoint cycles, and are known as 2-factors in graph theory [40] and as melts of rings in polymer physics [15, 16]. The second condition is the *single-loop condition*, which excludes configurations composed of multiple disconnected cycles and retains only those forming a single closed path (see Fig. 1, Panel d for a counterexample). Unlike the Hamiltonian condition, the single-loop condition concerns the connectivity of the multiloop. Since graph connectivity is not definable in first-order logic, it cannot be verified using any collection of purely local Boolean constraints. [22]. Consequently, we cannot define a local classical Hamiltonian encoding all the Hamiltonian cycles in its degenerate ground space, but, as we show in here, we can encode a coherent superposition of all the Hamiltonian cycles in the unique ground state of a suitable quantum system.

We proceed as follows. Each classical configuration of the dual lattice

$$\sigma = (\sigma_{1,1}, \dots, \sigma_{m+1,n+1}) \in \Sigma = \{-1, 1\}^{(m+1)(n+1)} \quad (1)$$

is mapped to a computational basis state $|\sigma\rangle$, and define the corresponding Hilbert space \mathcal{H} spanned by these basis states. Then we define a local, non-diagonal Hamiltonian \hat{H}_{HC} on \mathcal{H} whose unique ground state is the equal-amplitude superposition of all Hamiltonian cycles:

$$|X_{HC}\rangle := \sum_{\sigma \in X_{HC}} \frac{1}{\sqrt{|X_{HC}|}} |\sigma\rangle, \quad (2)$$

where X_{HC} is the set of all the dual-lattice configurations representing Hamiltonian cycles, and $|X_{HC}|$ is its cardinality.

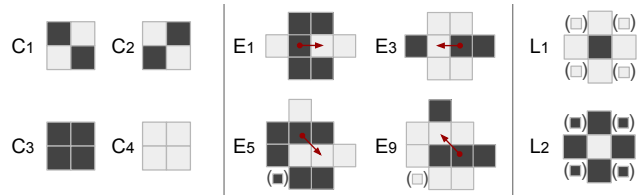


FIG. 3. *Local constraints and transformation rules involved in the definition of the Hamiltonian \hat{H}_{HC} .* **Panels C_1, C_2, C_3, C_4 :** local configurations forbidden in 2-factors. **Panels E_1, E_3, E_5, E_9 :** local transformations connecting the complete set of topologically equivalent 2-factors. The red arrow indicates the swap between two different color plaquettes, while the state of the other plaquettes remains unchanged. The missing transformations $\{E_2, E_4\}$ are obtained by rotating transformations E_1 and E_3 by 90 degrees. The missing transformations $\{E_6, E_7, E_8, E_{10}, E_{11}, E_{12}\}$ are obtained by rotating transformations E_5 and E_9 by 90, 180 and 270 degrees. Plaquettes shown in parentheses are not part of the corresponding rule or constraint, but are fixed in the displayed configuration as a consequence of the constraints C_1, C_2, C_3 , and C_4 . **Panels L_1, L_2 :** local configurations encoding local cycles.

We construct \hat{H}_{HC} as the sum of three local Hamiltonians:

$$\hat{H}_{HC} = \hat{H}_C + \hat{L}_E + \hat{H}_L, \quad (3)$$

where each term is frustration-free, and positive semidefinite, and enforces a distinct constraint on its ground states:

- $\text{Ker}(\hat{H}_C)$ spans states representing 2-factors;
- $\text{Ker}(\hat{L}_E)$ spans states assigning equal amplitude to topologically equivalent 2-factors; and
- $\text{Ker}(\hat{H}_L)$ spans states containing no cycles enclosing a single plaquette. We name these cycles local loops.

We will demonstrate that the kernel of \hat{H}_{HC} is spanned only by $|X_{HC}\rangle$, which is the only state that simultaneously satisfies all constraints. It follows that the total Hamiltonian is frustration free.

The remainder of this section is devoted to defining \hat{H}_C , \hat{L}_E , and \hat{H}_L , and characterizing their spectra and eigenstates (Fig. 2).

B. Definition of the Hamiltonian \hat{H}_C enforcing 2-factor configurations

Violations of the Hamiltonian condition can be ruled out by enforcing purely local constraints. A vertex (i, j) of the original lattice is traversed exactly once if and only if the four dual plaquettes surrounding it, $(i, j), (i, j+1), (i+1, j), (i+1, j+1)$, avoid the forbidden configurations C_1, C_2, C_3 , and C_4 shown in Fig. 3. Each

of these patterns corresponds to an invalid local arrangement in which the degree of vertex (i, j) , that is, the number of path edges incident on the vertex, differs from two. Hence, identifying 2-factors on the original lattice reduces to finding binary configurations of the dual lattice that simultaneously satisfy a set of local four-plaquette constraints excluding the forbidden configurations C_1 , C_2 , C_3 , and C_4 .

We map each forbidden four-plaquette pattern to a corresponding local diagonal operator, whose expectation value returns 1 to configurations violating the constraint within the block of plaquettes, and 0 to all others:

$$\begin{aligned} C_1 &\rightarrow \hat{C}_{ij}^{[1]} = \hat{P}_{ij}^{[0]} \hat{P}_{i,j+1}^{[0]} \hat{P}_{i+1,j}^{[0]} \hat{P}_{i+1,j+1}^{[0]} \\ C_2 &\rightarrow \hat{C}_{ij}^{[2]} = \hat{P}_{ij}^{[1]} \hat{P}_{i,j+1}^{[1]} \hat{P}_{i+1,j}^{[1]} \hat{P}_{i+1,j+1}^{[1]} \\ C_3 &\rightarrow \hat{C}_{ij}^{[3]} = \hat{P}_{ij}^{[0]} \hat{P}_{i,j+1}^{[1]} \hat{P}_{i+1,j}^{[1]} \hat{P}_{i+1,j+1}^{[0]} \\ C_4 &\rightarrow \hat{C}_{ij}^{[4]} = \hat{P}_{ij}^{[1]} \hat{P}_{i,j+1}^{[0]} \hat{P}_{i+1,j}^{[0]} \hat{P}_{i+1,j+1}^{[1]}, \end{aligned} \quad (4)$$

where $\hat{P}_{ij}^{[1]} := (|1\rangle\langle 1|)_{ij}$ and $\hat{P}_{ij}^{[0]} := (|0\rangle\langle 0|)_{ij}$. The sum of these operators yields the Hamiltonian

$$\hat{H}_C = \sum_{\substack{1 \leq i \leq m \\ 1 \leq j \leq n}} \left(C_{ij}^{[1]} + C_{ij}^{[2]} + C_{ij}^{[3]} + C_{ij}^{[4]} \right), \quad (5)$$

which is diagonal in the computational basis and counts the number of violations of the constraints. By construction, the ground states are degenerate, have zero energy, and encode all possible 2-factors.

C. Topological deformation rules

The single-loop condition is a topological property that depends on the global structure of the loops and cannot be detected by any finite set of local, diagonal constraints. Nevertheless, configurations that are *topologically equivalent* — i.e., configurations containing the same number of loops with the same nesting structure — can be transformed into one another through sequences of local deformations that neither cut nor merge loops. These deformations act as discrete analogues of homotopies, then preserving both the number of cycles and their nesting structure.

Building on this observation, we define a family of transformation rules that locally modify dual-lattice configurations. The full set of rules is:

$$E = \bigcup_{\substack{k \in [1,12] \\ 1 \leq i \leq m+2-w_k \\ 1 \leq j \leq n+2-h_k}} \left\{ e_{ij}^{[k]}, e_{ij}^{[k]-1} \right\}, \quad (6)$$

where

$$e_{ij}^{[k]} : \sigma \in \Sigma \rightarrow \sigma' \in \Sigma, \quad (7)$$

is a transformation rule acting on a block of $w_k \times h_k$ plaquettes whose upper-left corner is (i, j) , and $e_{ij}^{[k]-1}$ is

its inverse. Each rule is defined as follows: if the block matches the pattern shown in Panels E_k of Fig. 3, the rule swaps a black and a white plaquette along the red arrow, leaving all other plaquettes unchanged; otherwise, the rule is undefined on σ .

The set E satisfies two properties:

- a) *soundness*: every rule maps any 2-factor into a topologically equivalent 2-factor; and
- b) *completeness*: any pair of topologically equivalent 2-factors can be connected by a finite sequence of rules in E .

In this sense, E forms a *sound and complete equational theory* for topologically equivalent 2-factors. Soundness follows because no rule generates any of the forbidden patterns C_1 , C_2 , C_3 , and C_4 thereby preserving the Hamiltonian condition; moreover, each rule moves a plaquette to a region of the same color, deforming the loops without cutting or merging them, therefore preserving topology. Previous works [41–43] demonstrated the completeness of E for any pair of Hamiltonian cycles. Here, we conjecture that completeness also extends to any pair of topologically equivalent 2-factors.

It is important to note that the equivalence relation generated by E coincides with topological equivalence only within the subspace of 2-factors. For example, since all rules in E conserve the number of plaquettes in the state $\sigma_{ij} = 1$, they cannot connect two cycles enclosing regions of different areas, even though such cycles are topologically equivalent.

The configuration space Σ is partitioned into equivalence classes containing all and only elements that are connected by the rules in E . We name this partition S :

$$\begin{aligned} S &= \{X_{\text{HC}}, X_1, \dots, X_l, Z_1, \dots, Z_m\}, \\ \Sigma &= X_{\text{HC}} \cup X_1 \cup \dots \cup X_l \cup Z_1 \cup \dots \cup Z_m \\ A \cap B &= \emptyset \quad \forall A, B \in S, \end{aligned} \quad (8)$$

where X_{HC} contains all dual-lattice configurations encoding Hamiltonian cycles; each X_α contains configurations encoding topologically equivalent 2-factors with the same number of cycles $l_\alpha > 1$ and the same nesting structure; and each Z_β contains configurations violating the Hamiltonian condition but mutually connected by the rules in E .

D. From rules to operators

Each rule $e \in E$ is naturally associated with an operator \hat{e} encoding its action on the computational basis of \mathcal{H} . For a rule $e_{ij}^{[k]}$, defined on a block of plaquettes with upper-left corner (i, j) , the corresponding operator is

$$\hat{e}_{ij}^{[k]} = \sum_{\sigma} |e_{ij}^{[k]}(\sigma)\rangle \langle \sigma|, \quad (9)$$

and the operator encoding the inverse rule is

$$\hat{e}_{ij}^{[k]\dagger} = \sum_{\sigma} |\sigma\rangle \langle e_{ij}^{[k]}(\sigma) | = \sum_{\sigma} |e_{ij}^{[k]-1}(\sigma)\rangle \langle \sigma|, \quad (10)$$

where the sums run over all configurations σ for which the rule is defined, i.e., those matching the pattern in Panel E_k of Fig. 3. We denote the set of rule operators as

$$\mathcal{E} = \{\hat{e} \mid e \in E\}. \quad (11)$$

The explicit form of the operators \hat{e} is shown in Appendix A. We note that the operators inherit locality from the corresponding rules.

Since each configuration in Σ corresponds to a computational basis state, following Eq. 8, we can decompose the Hilbert space as a direct sum of corresponding orthogonal subspaces:

$$\mathcal{H} = \mathcal{X}_{\text{HC}} \oplus \mathcal{X}_1 \oplus \dots \oplus \mathcal{X}_l \oplus \mathcal{Z}_1 \oplus \dots \oplus \mathcal{Z}_m \quad (12)$$

where we define $\mathcal{A} = \text{span}(\{|\sigma\rangle \mid \sigma \in A\})$ for any set $A \in S$. The action of the rules in E generates each set $A \in S$, thus \mathcal{A} is the linear span of all states reachable from any $|\sigma\rangle \in A$ by applying the rule operators:

$$\mathcal{A} = \text{span}\left\{\hat{e}_{i_1} \dots \hat{e}_{i_m} |\sigma\rangle \mid m \in \mathbb{N}, \hat{e}_{i_j} \in \{\mathcal{E}\}\right\}. \quad (13)$$

E. Definition of a Hamiltonian \hat{L}_E enforcing equivalence between 2-factors.

Following the quantum equational reasoning framework in Ref. [25], we define the Laplacian Hamiltonian

$$\hat{L}_E = \sum_{k=1}^{12} \sum_{\substack{1 \leq i \leq m+2-w_k \\ 1 \leq j \leq n+2-h_k}} \left[\left(\hat{e}_{ij}^{[k]} + h.c. \right)^2 - \left(\hat{e}_{ij}^{[k]} + h.c. \right) \right], \quad (14)$$

where $\hat{e}_{ij}^{[k]}$ denotes the local operator implementing rule E_k , and $w_k \times h_k$ is the support of that rule.

The Hamiltonian \hat{L}_E is local and frustration-free. In the computational basis, \hat{L}_E is the discrete Laplacian of the graph G whose vertices represent dual-lattice configurations and whose edges correspond to applications of the rules in E . The graph G is disconnected, and each connected subgraph is an equivalence class $A \in S$. Following the decomposition of \mathcal{H} , the block-diagonal form of the Laplacian Hamiltonian is:

$$\hat{L}_E = \hat{L}_E|_{\mathcal{X}_{\text{HC}}} \oplus \dots \oplus \hat{L}_E|_{\mathcal{X}_l} \oplus \dots \oplus \hat{L}_E|_{\mathcal{Z}_m}, \quad (15)$$

where $\hat{L}_E|_{\mathcal{A}}$ is the Laplacian of the connected subgraph G_A . The ground state of each block is the zero-energy state given by the equal-amplitude superposition of all computational-basis states in the corresponding class:

$$|A\rangle := G.S.(\hat{L}_E|_{\mathcal{A}}) = \sum_{\sigma \in A} \frac{1}{\sqrt{|A|}} |\sigma\rangle. \quad (16)$$

The target state $|X_{\text{HC}}\rangle$ is the ground state that lies in \mathcal{X}_{HC} .

Within each subspace, the excited states are superpositions whose amplitudes satisfy discrete Laplace equations on the corresponding connected subgraph G_A . Thus, they are a graph generalisation of harmonic functions. The first excited state defines a bipartite clustering of G_A [44, 45] and the corresponding energy gap Δ_A may signal the presence of bottlenecks in G_A [44]. Finally, the mixing time τ_A of a random walk on G_A is inversely proportional to Δ_A [46].

F. Definition of a Hamiltonian \hat{H}_L enforcing no local cycles.

Here, we construct the Hamiltonian \hat{H}_L , whose kernel spans the configurations that do not contain any *local cycle*. Local cycles correspond to the patterns L_1 and L_2 in Fig. 3, each representing a loop enclosing a single plaquette.

As in the construction of \hat{H}_C , we associate to each forbidden pattern a local diagonal operator whose expectation value returns 1 over configurations with a local cycle, and 0 otherwise. For the block of plaquettes with upper-left corner (i, j) , we define:

$$\begin{aligned} L_1 \rightarrow \hat{L}_{ij}^{[1]} &= \hat{P}_{i,j+1}^{[0]} \hat{P}_{i+1,j}^{[0]} \hat{P}_{i+1,j+1}^{[1]} \hat{P}_{i+1,j+2}^{[0]} \hat{P}_{i+2,j+1}^{[0]} \\ L_2 \rightarrow \hat{L}_{ij}^{[2]} &= \hat{P}_{i,j+1}^{[1]} \hat{P}_{i+1,j}^{[1]} \hat{P}_{i+1,j+1}^{[0]} \hat{P}_{i+1,j+2}^{[1]} \hat{P}_{i+2,j+1}^{[1]}. \end{aligned} \quad (17)$$

Summing over all positions gives the local Hamiltonian:

$$\hat{H}_L = \sum_{\substack{1 \leq i \leq m-1 \\ 1 \leq j \leq n-1}} \left[\hat{L}_{ij}^{[1]} + \hat{L}_{ij}^{[2]} \right]. \quad (18)$$

Ground states of \hat{H}_L have zero energy and correspond to configurations without local cycles, i.e. no plaquette is enclosed by a unit-area loop. Configurations containing local cycles appear as excited states, with energy penalty proportional to the number of such cycles, and a minimum gap $\Delta_L = 1$. As we show in the next section, disjoint cycles enclosing more than a single plaquette are also penalized through the interplay between \hat{H}_L and \hat{L}_E .

G. Spectral properties of \hat{H}_{HC}

We now analyse the spectral properties of the total Hamiltonian defined as:

$$\hat{H}_{\text{HC}} = \hat{H}_C + \hat{H}_L + \hat{L}_E. \quad (19)$$

a. Block decomposition of \hat{H}_C . The Hamiltonian \hat{H}_C is block-diagonal in the space decomposition in Eq. 12. Because the rules in E preserve the Hamiltonian condition, i.e. $[\hat{C}_{ij}^{[k]}, \hat{e}_{i'j'}^{[l]}] = 0$, \hat{H}_C is constant on

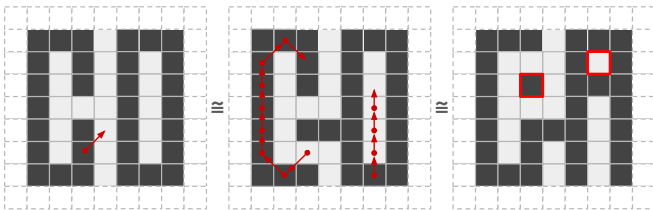


FIG. 4. *Contraction of a loop to a local loop.* Rules in E can be used to contract a 2-factor with more than one cycle to a 2-factor where innermost cycles enclose a single plaquette of the dual lattice.

each subspace:

$$\begin{aligned} \hat{H}_C &= \hat{H}_C|_{\mathcal{X}_{\text{HC}}} \oplus \cdots \oplus \hat{H}_C|_{\mathcal{X}_i} \oplus \cdots \oplus \hat{H}_C|_{\mathcal{Z}_m} \\ &= 0 \cdot \mathbf{1} \oplus \cdots \oplus 0 \cdot \mathbf{1} \oplus \cdots \oplus N_{\mathcal{Z}_m} \cdot \mathbf{1}, \end{aligned} \quad (20)$$

where no violation of the Hamiltonian condition happens in the equivalence classes $\mathcal{X}_{\text{HC}}, \dots, \mathcal{X}_i$ encoding 2-factors, and $N_{\mathcal{Z}_i} \geq 1$ counts the violations in any configuration in \mathcal{Z}_i .

b. Block decomposition of \hat{H}_L . Being itself diagonal, \hat{H}_L can be written with the same block structure:

$$\hat{H}_L = \hat{H}_L|_{\mathcal{X}_{\text{HC}}} \oplus \cdots \oplus \hat{H}_L|_{\mathcal{X}_i} \oplus \cdots \oplus \hat{H}_L|_{\mathcal{Z}_m}. \quad (21)$$

Since Hamiltonian cycles contain no local cycles, $\hat{H}_L|_{\mathcal{X}_{\text{HC}}} = 0 \cdot \mathbf{1}$. In contrast, by applying the deformation rules in E , any multi-loop 2-factor can be transformed into a configuration where at least one innermost cycle encloses a single plaquette, see Fig. 4. Thus, each equivalence class \mathcal{X}_α with $l_\alpha > 1$ — i.e., containing a 2-factor with more than one loop — includes configurations with a local cycle. As a consequence, \hat{H}_L is positive in each \mathcal{X}_i with $l_\alpha > 1$.

Combining Eqs. 15, 20, and 21, we can block-diagonalize the total Hamiltonian:

$$\begin{aligned} \hat{H}_{\text{HC}} &= \hat{L}_E|_{\mathcal{X}_{\text{HC}}} \oplus \cdots \oplus \left(\hat{L}_E + \hat{H}_L \right) \Big|_{\mathcal{X}_i} \\ &\oplus \cdots \oplus \left(N_{\mathcal{Z}_m} \cdot \mathbf{1} + \hat{L}_E + \hat{H}_L \right) \Big|_{\mathcal{Z}_m}. \end{aligned} \quad (22)$$

From the last decomposition, the spectral structure is thus clear:

- in the subspace \mathcal{X}_{HC} , the ground state is $|X_{\text{HC}}\rangle$, the first energy gap is the Laplacian gap $\Delta_{\mathcal{X}_{\text{HC}}}$, and excited states are harmonic superpositions of Hamiltonian cycles.
- Subspaces \mathcal{X}_α span superpositions of topologically equivalent 2-factors with more than one cycle, which include configurations penalized by \hat{H}_L . The ground state of $\hat{L}_E|_{\mathcal{X}_\alpha}$, which is the equal-amplitude superposition $|X_\alpha\rangle$, acquires energy proportional to the fraction of equivalent configurations containing at least one local cycle. As we show in Appendix B, this fraction scales as $1/(n \cdot m)$, and,

as a consequence of the Halmos' two-subspaces theorem [47, 48], the ground state energy in the sector \mathcal{X}_α is lower bounded by $\frac{\Delta_{\mathcal{X}_1}}{4mn(1+\Delta_{\mathcal{X}_1})}$.

- Finally, non-Hamiltonian cycles are encoded in the subspaces \mathcal{Z}_i . In these subspaces, the ground states have energy at least $N_{\mathcal{Z}_i} \geq 1$.

We conclude that \hat{H}_{HC} is a local, frustration-free Hamiltonian with a unique zero-energy ground state $|X_{\text{HC}}\rangle$. The first excited energy in each block is controlled either by the Laplacian gap of that block and, in the case of multiloop sectors \mathcal{X}_α , by the probability of encountering a local cycle within the class. The overall lower bound on the first energy gap reads:

$$\Delta \geq \min \left(\Delta_{\mathcal{X}_{\text{HC}}}, \frac{\Delta_{\mathcal{X}_1}}{4mn(1+\Delta_{\mathcal{X}_1})}, \dots, \frac{\Delta_{\mathcal{X}_i}}{4mn(1+\Delta_{\mathcal{X}_i})}, 1 \right). \quad (23)$$

III. POLYMERS AND HETEROPOLYMERS AT FINITE TEMPERATURE

If the energy $E_{\text{poly}}(\sigma)$ of a maximally compact polymer depends only on its spatial configuration σ , then the state $|X_{\text{HC}}\rangle$ represents the corresponding infinite temperature Boltzmann distribution. After preparing $|X_{\text{HC}}\rangle$, amplitude amplification enables accelerated estimation of classical expectation values over the ensemble of compact polymers, but also the estimation of quantities expressible as expectation values of non-diagonal operators, such as the partition function (see Appendix C). Appendix E illustrates with an example the use of amplitude amplification for expectation value estimation, and Ref. [24] provides a comprehensive overview of this methodology.

To generalize our approach to finite temperature, it is necessary to prepare a coherent quantum sample of the Boltzmann distribution $p(\sigma) = \sum_{\sigma \in X_{\text{HC}}} e^{-\beta E_{\text{poly}}(\sigma)} / Z(\beta)$, where $Z(\beta) = \sum_{\sigma \in X_{\text{HC}}} e^{-\beta E(\sigma)}$ is the partition function. The corresponding coherent quantum sample is

$$|Z(\beta)\rangle := \frac{1}{Z(\beta)} \sum_{\sigma \in X_{\text{HC}}} \sqrt{e^{-\beta E(\sigma)}} |\sigma\rangle. \quad (24)$$

This coherent sample can be prepared by evolving the state $|X_{\text{HC}}\rangle$ for an imaginary time $\beta/2$ using the classical Hamiltonian $\hat{H}_{\text{poly}} = \sum_{\sigma} E_{\text{poly}}(\sigma) |\sigma\rangle\langle\sigma|$. Implementing imaginary time evolution [32–35] yields

$$\frac{e^{-\frac{\beta}{2} \hat{H}_{\text{poly}}} |X_{\text{HC}}\rangle}{\left\| e^{-\frac{\beta}{2} \hat{H}_{\text{poly}}} |X_{\text{HC}}\rangle \right\|} = \frac{1}{Z(\beta)} \sum_{\sigma \in X_{\text{HC}}} e^{-\frac{\beta}{2} E(\sigma)} |\sigma\rangle = |Z(\beta)\rangle. \quad (25)$$

The Hamiltonian \hat{H}_{poly} assigns an energy to each polymer configuration based solely on its shape, as represented by a Hamiltonian cycle. However, this model

where the elements in the sum are pictorially described in Figure 5 Panel (a).

We construct a circuit of local operators $|X_{\text{HC}}\rangle \otimes |W_{c_1}\rangle$ evolving the initial state to the state $|D\rangle$. To this aim, we introduce local many-body unitaries $\hat{K}_{i,j}$, $\hat{M}_{i,j}$, $\hat{W}_{c,i,j}$, $\hat{V}_{c,i,j}$, and $\hat{Z}_{c,i,j}$, whose action on the computational basis states of the local subsystem is depicted in Figure 5 Panel (b).

The operators $\hat{K}_{i,j}$ and $\hat{M}_{i,j}$ act on pairs of empty characters that are adjacent to a monomer character along the Hamiltonian cycle. They replace the state $|\epsilon\epsilon\rangle$ of the two empty vertices with the superposition $(|t\epsilon\rangle + |\epsilon t\rangle)/\sqrt{2}$. The action of these operators over the entire lattice is illustrated in Fig. 5 Panel (c). The resulting state is a quantum superposition of Hamiltonian configurations in which the first monomer of the sequence is placed at every possible vertex, while a terminal character appears either before or after the monomer, thereby encoding the two possible orientations of the sequence.

The next step of the procedure consists of sequentially adding all monomers of the sequence to each configuration. This is achieved by applying the operators $\hat{W}_{c,i,j}$ and $\hat{V}_{c,i,j}$, which place the monomer character c on an empty vertex adjacent to an existing monomer along the Hamiltonian cycle. Acting with these operators over the entire lattice appends the character c to the next empty site along the Hamiltonian cycle, as illustrated in Fig. 5 Panel (d).

Once all monomers except the final one have been placed, the operator $\hat{Z}_{c,i,j}$ is applied to each lattice vertex, replacing the terminal character t with the last monomer of the sequence (see Fig. 5 Panel (d)).

In this way, we finally obtain a circuit capable of preparing the target state:

$$|D\rangle = \prod_{ij} \hat{Z}_{c_{mn},i,j} \left[\prod_{l \in \{mn-1, \dots, 2\}} \left(\prod_{ij} \hat{W}_{c_l, i, j} \hat{V}_{c_l, i, j} \right) \right] \prod_{ij} \hat{K}_{ij} \hat{M}_{i,j} (|X_{\text{HC}}\rangle \otimes |W_{c_1}\rangle). \quad (29)$$

IV. TENSOR NETWORK APPLICATIONS

In this section, we employ tensor network (TN) methods [37, 38, 49–51] to approximate the ground state of \hat{H}_{HC} on a dual lattice with $(m+1) \times (n+1)$ plaquettes, corresponding to an $m \times n$ rectangular lattice.

We encode the state $|X_{\text{HC}}\rangle$ as a *Matrix Product State* (MPS), a one-dimensional array of rank-3 tensors connected through contracted indices. Fig. 6 illustrates the mapping from the dual lattice to the MPS. Each tensor has at most a shape $(\chi, 2, \chi)$, where 2 is the dimension of the local Hilbert space and χ is the dimension of the contracted indices. The parameter χ , called the *bond dimension*, determines the accuracy of the MPS approximation. The 2D dual lattice is mapped to a 1D chain

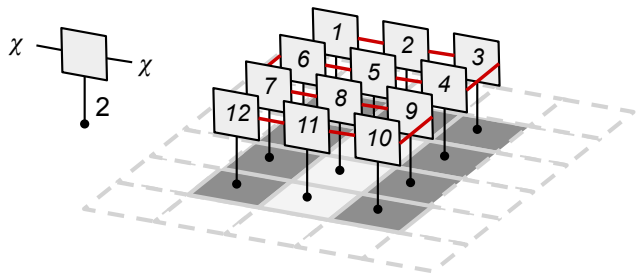


FIG. 6. *Encoding dual lattice configuration in a matrix product state.* Each plaquette in the bulk is associated with a rank-3 tensor. The tensors encoding plaquettes that are adjacent along a snake in the bulk are connected (red links).

using a snake space-filling curve [52]. Since all boundary plaquette states are fixed to $\sigma_{ij} = 0$, only the bulk $(n-1) \times (m-1)$ plaquettes need to be encoded in the MPS. The snake curve, therefore, starts from the top-left corner of the bulk, proceeds first along its shorter side, and covers all these sites, see Fig. 6.

We obtain the MPS representation of $|X_{\text{HC}}\rangle$ using the density matrix renormalization group (DMRG) algorithm [37], as implemented in the tensor-network emulator suite *Quantum TEA Leaves* [53]. We consider rectangular lattices of shape $6 \times n$ with n in the range [4, 40], and square lattices of shape $n \times n$ with even n in the range [4, 10]. For each lattice shape, we perform DMRG calculations with bond dimension $\chi \in [32, 64, 128, 256, 384]$.

This TN framework provides a compressed encoding of the entire ensemble of Hamiltonian cycles. Instead of explicitly storing all configurations, which would require exponential memory, the MPS represents the coherent quantum sample $|X_{\text{HC}}\rangle$ with a tractable bond dimension. This compact representation enables the efficient calculation of expectation values, and supports efficient sampling of Hamiltonian cycles [54], as well as their approximate counting. Indeed, as shown in Appendix C, the total number of Hamiltonian cycles is given by the expectation value

$$\langle X_{\text{HC}} | \bigotimes_{\substack{2 \leq i \leq m \\ 2 \leq j \leq n}} \hat{P}_{ij}^x | X_{\text{HC}} \rangle = \frac{|X_{\text{HC}}|}{2^{(m-1)(n-1)}}, \quad (30)$$

where P_i^x projects onto the positive eigenstate of the Pauli- X operator. Sampling the expectation value in Eq. 30 — either through classical Monte-Carlo methods or by measurements on a quantum computer — is extremely difficult due to the exponentially small fraction of Hamiltonian cycles.

In Fig. 7, we assess the quality of the MPS approximation of $|X_{\text{HC}}\rangle$ using several figures of merit for rectangular and square lattice geometries and different bond dimensions. Panels (a) and (b) show the energy of the MPS, i.e., the expectation value of the Hamiltonian \hat{H}_{HC} . Any energy larger than zero signals constraint violations as well as non-uniformity in the probability distribution

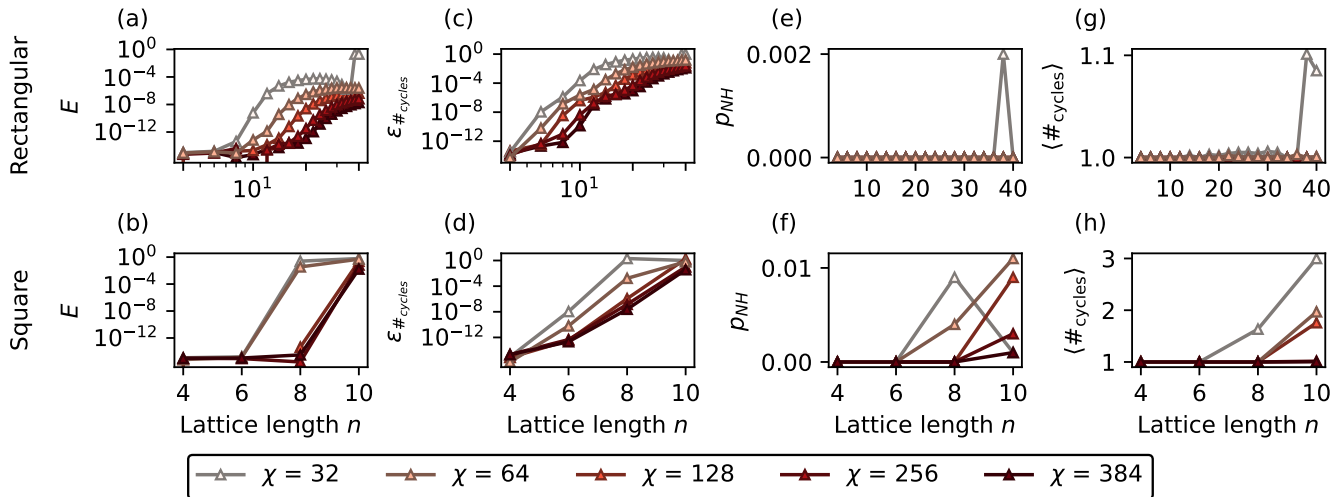


FIG. 7. *Quality of the MPS approximations of $|X_{\text{HC}}\rangle$ for different lattice lengths n and bond dimensions χ .* Panels (a,c,e,g) correspond to rectangular lattices of size $6 \times n$, while panels (b,d,f,h) correspond to square lattices of size $n \times n$. **Panels (a, b):** Tensor network state energy E ; the exact ground-state energy of H_{HC} is $E_0 = 0$ by construction. **Panels (c, d):** Relative error in the number of Hamiltonian cycles, measured as an observable and compared with exact values from Refs. [13, 14]. **Panels (e, f):** Probability of sampling non-Hamiltonian multiloops (from 1000 samples). **Panels (g, h):** Expected number of cycles in sampled configurations representing 2-factors (from 1000 samples).

encoded in the MPS. Panels (c) and (d) display the relative error

$$\varepsilon_{\#\text{cycles}} = \frac{||X_{\text{HC}}|^{\chi} - |X_{\text{HC}}|^{\text{exact}}|}{|X_{\text{HC}}|^{\text{exact}}} \quad (31)$$

where $|X_{\text{HC}}|^{\text{exact}}$ denotes the number of Hamiltonian cycles obtained via exact counting [13, 14], and $|X_{\text{HC}}|^{\chi}$ derives from Eq. 30. A small relative error indicates that the MPS successfully captures the full ensemble of Hamiltonian cycles. The exact and MPS-based counting results are also compared in Tables I and II, corresponding to rectangular and square lattices, respectively.

Panels (e) and (f) of Figure 7 report the probability of obtaining multiloop configurations that violate the Hamiltonian condition, estimated from 1000 samples drawn from the MPS. Finally, Panels (h) and (i) present the expectation value of the number of cycles obtained from the sampled 2-factor configurations. Since a Hamiltonian cycle contains exactly one loop, an exact MPS representation of $|X_{\text{HC}}\rangle$ yields an expected cycle count of 1. Deviations above 1, therefore mark contributions from multiloop 2-factors. Together, these last two measures quantify the quality of the MPS representation of the Hamiltonian-cycle ensemble.

As the bond dimension increases, all quality indicators in Figure 7 improve. For a fixed bond dimension and rectangular lattice, the approximation errors increase less than polynomially as the system size grows and tend towards a stable value. In contrast, for square lattices, the quality deteriorates rapidly with increasing system size and fixed bond dimension. The bond-dimension dependence of the approximation quality for fixed rectangular shapes is discussed in Appendix D, where we observe

that both the energy and the relative error in counting Hamiltonian cycles converge polynomially with the bond dimension, with the convergence rate decreasing as the system size increases. For square lattices instead, convergence only begins once the bond dimension exceeds a threshold value that grows rapidly with system size, preventing an efficient approximation.

The behavior of the quality factors in Fig. 7 reflects the entanglement structure of the state $|X_{\text{HC}}\rangle$. In Fig. 8, we plot the entanglement entropy of this state for various bipartitions along the snake-like ordering used to map the two-dimensional lattice onto a one-dimensional MPS. The entanglement entropy is normalized by the smaller lattice dimension m , which corresponds to the area of the bipartition boundary (see Panel (a)). Panel (b) shows results for lattices of fixed width $m = 6$ and lengths $n \in \{4, \dots, 10\}$, while Panel (c) displays data for square lattices with $n = m = L$ and $L \in \{4, 6, 8, 10\}$. In both cases, as the subsystem volume increases, the size of the boundary associated with the lattice bipartition remains fixed. The normalized entanglement S/m is nearly independent of both the subsystem volume v and the boundary size m , consistent with an area-law scaling of the entanglement entropy. Appendix D further analyzes the dependence of the maximum bipartition entanglement entropy on the bond dimension, confirming these indications of area-law scaling.

This area-law scaling admits a simple geometric interpretation. The distribution over Hamiltonian cycles on the full lattice differs from the product of the distributions restricted to two disjoint regions because any Hamiltonian cycle necessarily crosses the interface between them, thereby inducing correlations. The strength

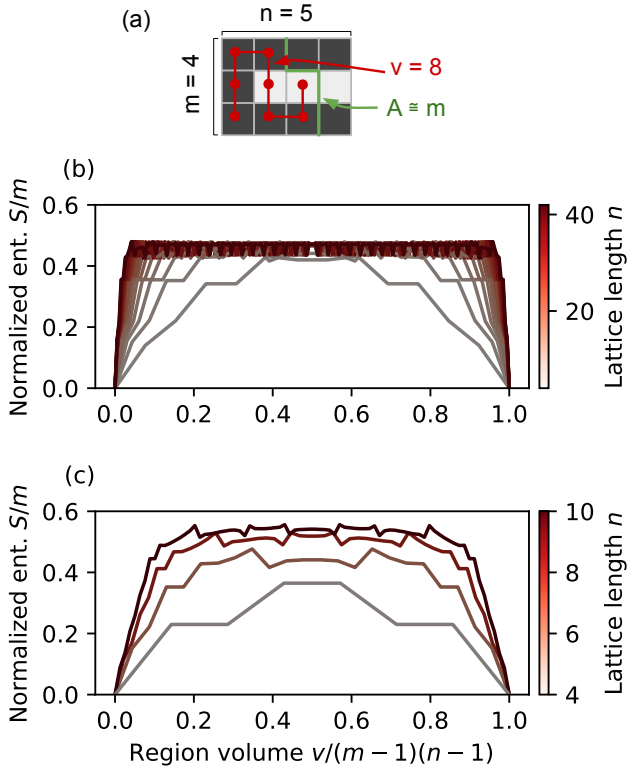


FIG. 8. Normalized entanglement entropy S calculated over bipartitions of a rectangular lattice. **Panel (a)**: the lattice shape is $m \times n$. The regions are defined by ordering the lattice sites along a snake path starting from the upper-left corner and selecting the first v sites. The size of the boundary between the region and the remainder of the system scales with the lattice width m . The entanglement entropy is normalized by m and is shown as a function of the ratio between the region size v and the dual lattice size $(m-1) \times (n-1)$, for lattices of different lengths n . **Panel (b)** corresponds to rectangular lattices with $m = 6$. **Panel (c)** corresponds to square lattices with $m = n$.

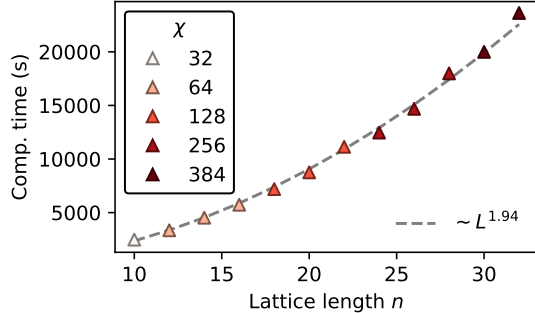


FIG. 9. Computational time needed for approximating $|X_{\text{HC}}\rangle$ on a rectangular lattice, as a function of the lattice length. We plot the time needed to construct an MPS approximation capable of encoding the total number of cycles with an error smaller than 0.5%. This takes into account both the required bond dimension (different colors of the markers) and the number of steps required for the DMRG algorithm to converge.

$m \times n$	$ X_{\text{HC}} ^{\chi=384}$	$ X_{\text{HC}} ^{\text{exact}}$	$\varepsilon_{\# \text{cycles}}$
6×4	37	37	0.0
6×6	1072	1072	0.0
6×8	32675	32675	0.0
6×10	1024028	1024028	0.0
6×12	32463805.26	32463802	1e-07
6×14	1033918048	1033917350	6.75e-07
6×16	3.298915608e+10	3.298906816e+10	2.67e-06
6×18	1.053352975e+12	1.053349394e+12	3.4e-06
6×20	3.364384982e+13	3.364354121e+13	9.17e-06
6×22	1.074721981e+15	1.074685815e+15	3.37e-05
6×24	3.433550978e+16	3.433060709e+16	0.000143
6×26	1.097166749e+18	1.096704136e+18	0.000422
6×28	3.506935385e+19	3.50348837e+19	0.000983
6×30	1.121357798e+21	1.119214053e+21	0.00191
6×32	3.587177531e+22	3.575412358e+22	0.00328
6×34	1.147992622e+24	1.142192547e+24	0.00505
6×36	3.675615823e+25	3.648821244e+25	0.00729
6×38	1.177146356e+27	1.165643875e+27	0.00977
6×40	3.771580754e+28	3.723738685e+28	0.0127

TABLE I. Number of Hamiltonian cycles for different shapes of a rectangular lattice. Comparison between exact counting $|X_{\text{HC}}|^{\text{exact}}$ [13, 14] and expectation value $|X_{\text{HC}}|^{\chi=384} = \langle X_{\text{HC}} | \bigotimes_{\substack{2 \leq i < m \\ 2 \leq j \leq n}} 2\hat{P}_{ij}^x | X_{\text{HC}} \rangle$ for bond dimension $\chi = 384$. Digits that differ from the exact values are highlighted in bold. $\varepsilon_{\# \text{cycles}}$ is the relative error of the expectation value with respect to the exact counting, whose scaling is depicted in Figure 7 Panel (c).

of these correlations is controlled by the number of boundary crossings, which is upper-bounded by the boundary area.

The observed area-law entanglement implies that the bond dimension required for an accurate MPS approximation is independent of the lattice's longer side and grows exponentially only with its shorter dimension. Consequently, the computational cost of constructing and manipulating the MPS is exponential in the smaller lattice dimension. Differently, as shown in Figure 9, when this dimension is fixed, we can approximate the entire Hamiltonian cycle ensemble in time that scales quadratically with the lattice length. Notably, the resulting MPS representation provides a compressed representation of the entire ensemble of Hamiltonian cycles. In this case, we are able to encode up to approximately 3.77×10^{28} Hamiltonian cycles within an MPS requiring only 380 MB of memory.

V. CONCLUSIONS AND OUTLOOK

We have constructed a local, frustration-free Hamiltonian whose unique ground state is a coherent quantum sample encoding the complete set of Hamiltonian cycles on a rectangular lattice. The construction relies on local constraints enforcing the Hamiltonian condition together with a family of topology-preserving local transformation rules. These ingredients make it possible to encode

$m \times n$	$ X_{\text{HC}} ^{\chi=384}$	$ X_{\text{HC}} ^{\text{exact}}$	$\varepsilon_{\#\text{cycles}}$
4×4	6	6	0.0
6×6	1072	1072	0.0
8×8	4638576. 113	4638576	2.44e-08
10×10	4.842640256e+11	4.672604566e+11	0.0351

TABLE II. Number of Hamiltonian cycles for different sizes of a square lattice. Comparison between exact counting $|X_{\text{HC}}|^{\text{exact}}$ [13, 14] and expectation value $|X_{\text{HC}}|^{\chi=384} = \langle X_{\text{HC}} | \bigotimes_{\substack{2 \leq i \leq m \\ 2 \leq j \leq n}} 2\hat{P}_{ij}^x | X_{\text{HC}} \rangle$ for bond dimension $\chi = 384$. Digits that differ from the exact values are highlighted in bold. $\varepsilon_{\#\text{cycles}}$ is the relative error of the expectation value with respect to the exact counting, whose scaling is depicted in Figure 7 Panel (d).

a highly non-local combinatorial property—the existence of a Hamiltonian cycle—into the ground state of a local quantum Hamiltonian.

This approach improves on formulations based on classical Hamiltonians, where enforcing global topological constraints requires an exponentially large number of non-local terms. By encoding the desired ensemble in a coherent quantum superposition rather than in a degenerate manifold of classical configurations, this strategy enables a quadratic speedup over classical Monte Carlo through the application of amplitude amplification on the ensemble of Hamiltonian cycles [23, 55]. We have further shown how to extend this strategy to encode Boltzmann distributions at finite temperature for both polymers and heteropolymers.

Restricting the analysis to two-dimensional closed paths simplified both the analytical construction of the Hamiltonian and the numerical approximation of the ground state. Nevertheless, the proposed framework applies to more general polymer ensembles, which can be represented by open Hamiltonian paths on a three-dimensional lattice. Specifically, the equational reasoning [25] approach to constructing the parent Hamiltonian is feasible whenever a complete and sound set of transformation rules exists to connect all and only the feasible polymer configurations. In the Monte Carlo literature, such a set is employed to explore polymer configurations ergodically [12]. Any relevant speedup in the computation of the partition function for a given heteropolymer sequence may prove invaluable in the context of protein design [56].

We have also shown that MPS provide accurate approximations of the entire ensemble of Hamiltonian cycles when one lattice dimension is fixed. This representation enables the approximate counting of Hamiltonian cycles through tensor-network contractions. In particular, the tensor-network approach allows the computation of expectation values that are inaccessible to classical Monte-Carlo, such as the probability of encountering a specific configuration. As a result, tensor-network methods offer a polynomial-time alternative for quasi-1D geometries and remain competitive for moderately sized two-dimensional lattices.

The tensor network method introduced in this study represents a generalization of transfer matrix methods. While transfer matrix methods are considered state-of-the-art for exact counting [13, 14], matrix product states enable the approximation of expectation values for arbitrary product operators. Similar to transfer matrix methods, these expectation values are computed by multiplying transfer matrices, which are formed by contracting each local tensor in the matrix product state with the corresponding local observable. This analogy also applies to computational time: due to area-law entanglement, both the proposed approach and standard transfer matrix methods demonstrate an exponential increase in transfer matrix dimension and runtime relative to the shorter dimension of the lattice. In contrast to transfer matrix methods, which construct the transfer matrix based on combinatorial principles, the present approach utilizes density matrix renormalization to economize computational resources, accepting a less accurate approximation, for example, by employing a small bond dimension.

In the future, a comprehensive understanding of the complexity of ground-state preparation will be essential for evaluating the full extent of quantum advantage. While we did not assess particular preparation strategies in this work, we note that quantum walk dynamics [57] is a good candidate for this purpose, since it can achieve a quadratic speedup in generating coherent quantum samples compared to classical Monte Carlo methods [24].

ACKNOWLEDGMENTS

We acknowledge M. Baiesi, M. Ballarin, M. Rigobello, M. Tesoro, A. Braghetto, E. Orlandini, and G. Cataldi for useful discussions. The research leading to these results has received funding from the following organizations: European Union via Italian Research Center on HPC, Big Data and Quantum Computing (NextGenerationEU Project No. CN00000013), project EuRyQa (Horizon 2020), project PASQuanS2 (Quantum Technology Flagship); Italian Ministry of University and Research (MUR) via: Quantum Frontiers (the Departments of Excellence 2023-2027); the World Class Research Infrastructure - Quantum Computing and Simulation Center (QCSC) of Padova University; Istituto Nazionale di Fisica Nucleare (INFN): iniziativa specifica IS-QUANTUM; the German Federal Ministry of Education and Research (BMBF) via the project QRydDemo. We acknowledge computational resources from Cloud Veneto, as well as computational time on Cineca’s Leonardo machine.

Appendix A: Operators encoding the action of rules in \mathcal{E}

Here we list the operators encoding the action of rules in \mathcal{E} . These operators are:

$$\begin{aligned}
E_1 &\rightarrow \hat{e}_{ij}^{[1]} = \hat{P}_{i,j+1}^{[1]} \hat{P}_{i,j+2}^{[1]} \hat{P}_{i+1,j}^{[0]} \hat{\sigma}_{i+1,j+1}^+ \hat{\sigma}_{i+1,j+2}^- \hat{P}_{i+1,j+3}^{[0]} \\
&\quad \otimes \hat{P}_{i+2,j+1}^{[1]} \hat{P}_{i+2,j+2}^{[1]} \\
E_2 &\rightarrow \hat{e}_{ij}^{[2]} = \mathcal{R} \left[e_{ij}^{[1]} \right] \\
E_3 &\rightarrow \hat{e}_{ij}^{[3]} = \hat{P}_{i,j+1}^{[0]} \hat{P}_{i,j+2}^{[0]} \hat{P}_{i+1,j}^{[1]} \hat{\sigma}_{i+1,j+1}^+ \hat{\sigma}_{i+1,j+2}^- \hat{P}_{i+1,j+3}^{[1]} \\
&\quad \otimes \hat{P}_{i+2,j+1}^{[0]} \hat{P}_{i+2,j+2}^{[0]} \\
E_4 &\rightarrow \hat{e}_{ij}^{[4]} = \mathcal{R} \left[e_{ij}^{[3]} \right] \\
E_5 &\rightarrow \hat{e}_{ij}^{[5]} = \hat{P}_{i,j+1}^{[0]} \hat{P}_{i+1,j}^{[1]} \hat{\sigma}_{i+1,j+1}^+ \hat{P}_{i+1,j+2}^{[1]} \hat{P}_{i+2,j}^{[1]} \hat{P}_{i+2,j+1}^{[0]} \\
&\quad \otimes \hat{\sigma}_{i+2,j+2}^- \hat{P}_{i+2,j+3}^{[0]} \hat{P}_{i+3,j+1}^{[1]} \hat{P}_{i+3,j+2}^{[1]} \\
E_6 &\rightarrow \hat{e}_{ij}^{[6]} = \mathcal{R} \left[e_{ij}^{[5]} \right] \\
E_7 &\rightarrow \hat{e}_{ij}^{[7]} = \mathcal{R} \left[e_{ij}^{[6]} \right] \\
E_8 &\rightarrow \hat{e}_{ij}^{[8]} = \mathcal{R} \left[e_{ij}^{[7]} \right] \\
E_9 &\rightarrow \hat{e}_{ij}^{[9]} = \hat{P}_{i,j+1}^{[1]} \hat{P}_{i+1,j}^{[0]} \hat{\sigma}_{i+1,j+1}^+ \hat{P}_{i+1,j+2}^{[0]} \hat{P}_{i+2,j}^{[0]} \hat{P}_{i+2,j+1}^{[1]} \\
&\quad \otimes \hat{\sigma}_{i+2,j+2}^- \hat{P}_{i+2,j+3}^{[1]} \hat{P}_{i+3,j+1}^{[0]} \hat{P}_{i+3,j+2}^{[0]} \\
E_{10} &\rightarrow \hat{e}_{ij}^{[10]} = \mathcal{R} \left[e_{ij}^{[9]} \right] \\
E_{11} &\rightarrow \hat{e}_{ij}^{[11]} = \mathcal{R} \left[e_{ij}^{[10]} \right] \\
E_{12} &\rightarrow \hat{e}_{ij}^{[12]} = \mathcal{R} \left[e_{ij}^{[11]} \right], \tag{A1}
\end{aligned}$$

where $\hat{P}_{ij}^{[0]} = (|0\rangle\langle 0|)_{ij}$, $\hat{P}_{ij}^{[1]} = (|1\rangle\langle 1|)_{ij}$, $\hat{\sigma}_{ij}^+ = (|1\rangle\langle 0|)_{ij}$, and $\hat{\sigma}_{ij}^- = (|0\rangle\langle 1|)_{ij}$. The super-operator \mathcal{R} rotates the region of the dual lattice on which a rule acts by $\pi/2$.

Appendix B: First energy gap of \hat{H}_{HC}

In this appendix, we study the scaling of the first non-zero eigenvalue Δ_α of the Hamiltonian \hat{H}_{HC} restricted to the orthogonal subspace \mathcal{X}_α .

1. Halmos's two-spaces theorem and the first energy gap

From Eq. 22, the Hamiltonian \hat{H}_{HC} restricted to \mathcal{X}_α can be written as

$$\hat{H}_{\text{HC}} \Big|_{\mathcal{X}_\alpha} = \left(\hat{L}_E + \hat{H}_L \right) \Big|_{\mathcal{X}_\alpha}. \tag{B1}$$

Let L_α (L_α^\perp) and N_α (N_α^\perp) denote, respectively, the

images (kernels) of \hat{L}_E and \hat{H}_L restricted to \mathcal{X}_α :

$$\begin{aligned}
L_\alpha &:= \ker \left(\hat{L}_E \right)^\perp \cap \mathcal{X}_\alpha \\
L_\alpha^\perp &:= \ker \left(\hat{L}_E \right) \cap \mathcal{X}_\alpha \\
N_\alpha &:= \ker \left(\hat{H}_L \right)^\perp \cap \mathcal{X}_\alpha \\
N_\alpha^\perp &:= \ker \left(\hat{H}_L \right) \cap \mathcal{X}_\alpha, \tag{B2}
\end{aligned}$$

where, with a slight abuse of notation, the orthogonal complements on the left-hand side are taken within \mathcal{X}_α , while those on the right-hand side are taken in the full Hilbert space \mathcal{H} .

By construction (see main text):

- L_α^\perp is spanned by the equal-weight superposition $|X_\alpha\rangle$ of all computational basis states encoding elements of X_α ;
- N_α^\perp is spanned by all computational basis states encoding elements of X_α that contain no local loops.

$|X_\alpha\rangle$ overlaps configurations both with and without local cycles. Hence, it is not contained in N_α^\perp , and

$$L_\alpha^\perp \cap N_\alpha^\perp = \emptyset. \tag{B3}$$

Let \hat{P}_α and \hat{Q}_α denote the projectors from \mathcal{X}_α onto the subspaces L_α and N_α , respectively; and let $\Delta_{\mathcal{X}_\alpha}$ and $\Delta_{L,\alpha}$ respectively be the smallest non-zero eigenvalues of $\hat{L}_E|_{\mathcal{X}_\alpha}$ and $\hat{H}_L|_{\mathcal{X}_\alpha}$. We then have

$$\begin{aligned}
\langle \psi | \hat{L}_E + \hat{H}_L | \psi \rangle &= \langle \psi | \hat{L}_E | \psi \rangle + \langle \psi | \hat{H}_L | \psi \rangle \\
&\geq \langle \psi | \Delta_{\mathcal{X}_\alpha} \hat{P}_\alpha | \psi \rangle + \langle \psi | \Delta_{L,\alpha} \hat{Q}_\alpha | \psi \rangle \\
&= \langle \psi | (\Delta_{\mathcal{X}_\alpha} \hat{P}_\alpha + \Delta_{L,\alpha} \hat{Q}_\alpha) | \psi \rangle \tag{B4}
\end{aligned}$$

for all $|\psi\rangle \in \mathcal{X}_\alpha$, so that the smallest eigenvalue of $(\hat{L}_E + \hat{H}_L) \Big|_{\mathcal{X}_\alpha}$ is bounded below by the smallest eigenvalue λ_α of $\Delta_{\mathcal{X}_\alpha} \hat{P}_\alpha + \Delta_{L,\alpha} \hat{Q}_\alpha$:

$$\begin{aligned}
\Delta_\alpha &= \min_{|\psi\rangle \in \mathcal{X}_\alpha} \frac{\langle \psi | \hat{L}_E + \hat{H}_L | \psi \rangle}{\langle \psi | \psi \rangle} \\
&\geq \min_{|\psi\rangle \in \mathcal{X}_\alpha} \frac{\langle \psi | (\Delta_{\mathcal{X}_\alpha} \hat{P}_\alpha + \Delta_{L,\alpha} \hat{Q}_\alpha) | \psi \rangle}{\langle \psi | \psi \rangle} := \lambda_\alpha. \tag{B5}
\end{aligned}$$

The spectral structure of the operator $\Delta_{\mathcal{X}_\alpha} \hat{P}_\alpha + \Delta_{L,\alpha} \hat{Q}_\alpha$ can be analyzed using Halmos's two-subspaces theorem.

Theorem 1 Halmos's two-subspaces theorem [47, 48]: *Let \hat{P}_α and \hat{Q}_α be the projectors onto subspaces L_α and N_α , respectively. Then, the Hilbert space \mathcal{X}_α can be decomposed as*

$$\mathcal{X}_\alpha = L_\alpha \cap N_\alpha \oplus L_\alpha \cap N_\alpha^\perp \oplus L_\alpha^\perp \cap N_\alpha \oplus L_\alpha^\perp \cap N_\alpha^\perp \oplus M_i \tag{B6}$$

and \hat{P}_α and \hat{Q}_α are block-diagonal in this decomposition. In particular, they can be written as

$$\hat{P}_\alpha = \mathbf{1} \oplus \mathbf{1} \oplus 0 \oplus 0 \oplus \begin{pmatrix} \mathbf{1} & 0 \\ 0 & 0 \end{pmatrix}, \quad (\text{B7})$$

$$\hat{Q}_\alpha = \mathbf{1} \oplus 0 \oplus \mathbf{1} \oplus 0 \oplus \begin{pmatrix} \mathbf{1} - S_\alpha^2 & S_\alpha \sqrt{\mathbf{1} - S_\alpha^2} \\ S_\alpha \sqrt{\mathbf{1} - S_\alpha^2} & S_\alpha^2 \end{pmatrix}, \quad (\text{B8})$$

for some Hermitian operator S_α^2 satisfying

$$0 \leq S_\alpha^2 \leq \mathbf{1}. \quad (\text{B9})$$

Since $L_\alpha^\perp \cap N_\alpha^\perp = \emptyset$, this component can be omitted from the decomposition. The Halmos' theorem then yields the following block-diagonal form for $\Delta_{\mathcal{X}_\alpha} \hat{P}_\alpha + \Delta_{L,\alpha} \hat{Q}_\alpha$:

$$\begin{aligned} \Delta_{\mathcal{X}_\alpha} \hat{P}_\alpha + \Delta_{L,\alpha} \hat{Q}_\alpha &= (\Delta_{\mathcal{X}_\alpha} + \Delta_{L,\alpha}) \mathbf{1} \oplus \Delta_{\mathcal{X}_\alpha} \mathbf{1} \\ &\oplus \Delta_{L,\alpha} \mathbf{1} \\ &\oplus \begin{pmatrix} (\Delta_{\mathcal{X}_\alpha} + \Delta_{L,\alpha}) \mathbf{1} - \Delta_{L,\alpha} S_\alpha^2 & \Delta_{L,\alpha} S_\alpha \sqrt{\mathbf{1} - S_\alpha^2} \\ \Delta_{L,\alpha} S_\alpha \sqrt{\mathbf{1} - S_\alpha^2} & \Delta_{L,\alpha} S_\alpha^2 \end{pmatrix}. \end{aligned} \quad (\text{B10})$$

The eigenvalues $\{x\}$ of $\Delta_{\mathcal{X}_\alpha} \hat{P}_\alpha + \Delta_{L,\alpha} \hat{Q}_\alpha$ can be found by imposing the eigenvalues equation on the Halmos' decomposition in Eq.B10:

$$\begin{aligned} \det \left[\Delta_{\mathcal{X}_\alpha} \hat{P}_\alpha + \Delta_{L,\alpha} \hat{Q}_\alpha - x \mathbf{1} \right] &= \\ (\Delta_{\mathcal{X}_\alpha} + \Delta_{L,\alpha} - x)^{\dim(L_\alpha \cap N_\alpha)} &\cdot (\Delta_{\mathcal{X}_\alpha} - x)^{\dim(L_\alpha \cap N_\alpha^\perp)} \cdot (\Delta_{L,\alpha} - x)^{\dim(L_\alpha^\perp \cap N_\alpha)} \\ \cdot \det \begin{pmatrix} (\Delta_{\mathcal{X}_\alpha} + \Delta_{L,\alpha} - x) \mathbf{1} - \Delta_{L,\alpha} S_\alpha^2 & \Delta_{L,\alpha} S_\alpha \sqrt{\mathbf{1} - S_\alpha^2} \\ \Delta_{L,\alpha} S_\alpha \sqrt{\mathbf{1} - S_\alpha^2} & \Delta_{L,\alpha} S_\alpha^2 - x \mathbf{1} \end{pmatrix} & \\ = 0. & \end{aligned} \quad (\text{B11})$$

The last determinant in the latter equation can be determined via the Schur complement formula, taking into account that the blocks of the matrix commute, so that we obtain

$$\begin{aligned} \det \begin{pmatrix} (\Delta_{\mathcal{X}_\alpha} + \Delta_{L,\alpha} - x) \mathbf{1} - \Delta_{L,\alpha} S_\alpha^2 & \Delta_{L,\alpha} S_\alpha \sqrt{\mathbf{1} - S_\alpha^2} \\ \Delta_{L,\alpha} S_\alpha \sqrt{\mathbf{1} - S_\alpha^2} & \Delta_{L,\alpha} S_\alpha^2 - x \mathbf{1} \end{pmatrix} & \\ = \det \left([(\Delta_{\mathcal{X}_\alpha} + \Delta_{L,\alpha} - x) \mathbf{1} - \Delta_{L,\alpha} S_\alpha^2] (\Delta_{L,\alpha} S_\alpha^2 - x \mathbf{1}) - \right. & \\ \left. (\Delta_{L,\alpha} S_\alpha \sqrt{\mathbf{1} - S_\alpha^2})^2 \right) & \\ = \det (x^2 - x(\Delta_{\mathcal{X}_\alpha} + \Delta_{L,\alpha}) + \Delta_{\mathcal{X}_\alpha} \Delta_{L,\alpha} S_\alpha^2) & \\ = \prod_{s_i \in \sigma(S_\alpha)} \left[x - \frac{(\Delta_{\mathcal{X}_\alpha} + \Delta_{L,\alpha}) \pm \sqrt{(\Delta_{\mathcal{X}_\alpha} + \Delta_{L,\alpha})^2 - 4\Delta_{\mathcal{X}_\alpha} \Delta_{L,\alpha} S_\alpha^2}}{2} \right], & \end{aligned} \quad (\text{B12})$$

where $\sigma(S_\alpha)$ is the spectrum of S_α .

The smallest eigenvalue is thus

$$\lambda_\alpha = \min \left(\Delta_{\mathcal{X}_\alpha}, \Delta_{L,\alpha}, \frac{(\Delta_{\mathcal{X}_\alpha} + \Delta_{L,\alpha}) - \sqrt{(\Delta_{\mathcal{X}_\alpha} + \Delta_{L,\alpha})^2 - 4\Delta_{\mathcal{X}_\alpha} \Delta_{L,\alpha} \|S_\alpha^2\|}}{2} \right). \quad (\text{B13})$$

Taking into account Eq. B9 we can write

$$\begin{aligned} (\Delta_{\mathcal{X}_\alpha} + \Delta_{L,\alpha}) - \sqrt{(\Delta_{\mathcal{X}_\alpha} + \Delta_{L,\alpha})^2 - 4\Delta_{\mathcal{X}_\alpha} \Delta_{L,\alpha} \|S_\alpha^2\|} & \\ \leq (\Delta_{\mathcal{X}_\alpha} + \Delta_{L,\alpha}) - \sqrt{(\Delta_{\mathcal{X}_\alpha} - \Delta_{L,\alpha})^2} & \\ = \min(2\Delta_{\mathcal{X}_\alpha}, 2\Delta_{L,\alpha}), & \end{aligned} \quad (\text{B14})$$

so that Eq. B13 reduces to

$$\lambda_\alpha = \frac{(\Delta_{\mathcal{X}_\alpha} + \Delta_{L,\alpha}) - \sqrt{(\Delta_{\mathcal{X}_\alpha} + \Delta_{L,\alpha})^2 - 4\Delta_{\mathcal{X}_\alpha} \Delta_{L,\alpha} \|S_\alpha^2\|}}{2}. \quad (\text{B15})$$

To evaluate $\|S_\alpha^2\|$, consider the operator \hat{R}_α , expressed in the Halmos decomposition as

$$\hat{R}_\alpha = 0 \oplus 0 \oplus 0 \oplus \begin{pmatrix} 0 & 0 \\ 0 & \mathbf{1} \end{pmatrix}. \quad (\text{B16})$$

This operator projects onto $M \cap L^\perp$.

Using the decomposition of \hat{Q}_α , we have

$$\hat{R}_\alpha \hat{Q}_\alpha \hat{R}_\alpha = 0 \oplus 0 \oplus 0 \oplus \begin{pmatrix} 0 & 0 \\ 0 & S_\alpha^2 \end{pmatrix}. \quad (\text{B17})$$

The corresponding norm can be expressed in the bra-ket formalism. The subspace $M \cap L^\perp$ consists of states lying in L^\perp that belong neither to N nor to N^\perp . These correspond to equal-amplitude superpositions over sets of topologically equivalent 2-factors that can be contracted to local loops or expanded to non-local ones. The only state in \mathcal{X}_α satisfying this condition is $|X_\alpha\rangle$, so that $\hat{R}_\alpha = |X_\alpha\rangle\langle X_\alpha|$ and

$$\|S_\alpha^2\| = \|\hat{R}_\alpha \hat{Q}_\alpha \hat{R}_\alpha\| = \langle X_\alpha | \hat{Q}_\alpha | X_\alpha \rangle. \quad (\text{B18})$$

Substituting the latter equation into Eq. B15, we obtain

$$\lambda_\alpha = \frac{\Delta_{\mathcal{X}_\alpha} + \Delta_{L,\alpha}}{2} - \sqrt{\left(\frac{\Delta_{\mathcal{X}_\alpha} + \Delta_{L,\alpha}}{2} \right)^2 - \Delta_{\mathcal{X}_\alpha} \Delta_{L,\alpha} \cdot \langle X_\alpha | \hat{Q}_\alpha | X_\alpha \rangle}. \quad (\text{B19})$$

2. Lower bound for $\langle X_\alpha | \hat{Q}_\alpha | X_\alpha \rangle$

We now aim to lower-bound the expectation value

$$\langle X_\alpha | \hat{Q}_\alpha | X_\alpha \rangle. \quad (\text{B20})$$

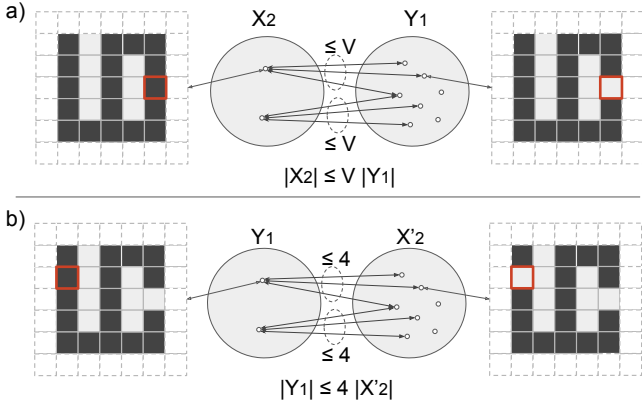


FIG. 10. Relation between the size of the set X_α of topologically equivalent 2-factors and its subset X'_α containing configurations with at least one local loop. The set $Y_{l_\alpha-1}$ denotes all possible 2-factors with $l_\alpha - 1$ cycles, where l_α is the number of cycles for the configurations in X_α . **Panel (a):** Configurations in X_α can be obtained by changing the color of a single plaquette belonging to the set $Y_{l_\alpha-1}$. **Panel (b):** Configurations in $Y_{l_\alpha-1}$ can be obtained by changing the color of a single plaquette in a configuration belonging to X'_α , here the modified plaquette is adjacent to a local cycle.

Recall that \hat{Q}_α is a projector on the rank of $\hat{H}_L|_{\mathcal{X}_\alpha}$, so it assigns the eigenvalue 0 to configurations that do not contain local loops, and 1 to those that contain one or more local loops. Let $X'_\alpha \subset X_\alpha$ denote the subset of configurations in X_α that contain at least one local loop. Then,

$$\langle X_\alpha | \hat{Q}_\alpha | X_\alpha \rangle = \sum_{\substack{\sigma, \sigma' \in X_\alpha \\ \sigma'' \in X'_\alpha}} \frac{1}{|X_\alpha|} \langle \sigma | \sigma'' \rangle \langle \sigma'' | \sigma' \rangle = \frac{|X'_\alpha|}{|X_\alpha|}, \quad (\text{B21})$$

that is, $\langle X_\alpha | \hat{Q}_\alpha | X_\alpha \rangle$ represents the fraction of topologically equivalent 2-factors that contain at least one local cycle.

We can bound this fraction using the following argument. Let $Y_{l_\alpha-1}$ be the set of all possible 2-factors containing $l_\alpha - 1$ cycles, where l_α is the number of cycles of the configurations in X_α . Every element of X_α can be obtained from some element of $Y_{l_\alpha-1}$ by changing the color of a single plaquette in the dual lattice (Fig. 10a). If V denotes the number of plaquettes in the lattice, this defines a mapping $Y_{l_\alpha-1} \leftrightarrow X_\alpha$ such that each configuration in X_α is connected to at least one and at most V configurations in $Y_{l_\alpha-1}$. This implies

$$|X_\alpha| \leq |Y_{l_\alpha-1}| \cdot V. \quad (\text{B22})$$

Analogously, each configuration in $Y_{l_\alpha-1}$ can be generated from one configuration in X'_α by merging a local loop with one of its adjacent loops. This operation is equivalent to changing the color of a single plaquette in the dual lattice, as discussed in the main text. In this case,

the plaquette must be adjacent to a local loop (Fig. 10b). Since each local loop has at most four adjacent plaquettes, this defines a mapping $X'_\alpha \leftrightarrow Y_{l_\alpha-1}$ such that each configuration in $Y_{l_\alpha-1}$ is connected to at least one and at most four configurations in X'_α . Hence,

$$|Y_{l_\alpha-1}| \leq 4 |X'_\alpha|. \quad (\text{B23})$$

Combining Eqs. B22 and B23, we find

$$\langle X_\alpha | \hat{Q}_\alpha | X_\alpha \rangle = \frac{|X'_\alpha|}{|X_\alpha|} \geq \frac{|Y_{l_\alpha-1}|}{|Y_{l_\alpha-1}| \cdot 4V} = \frac{1}{4V}. \quad (\text{B24})$$

Substituting this bound into Eq. B19 yields

$$\lambda_\alpha \geq \frac{1}{2} \left(\Delta_{\mathcal{X}_\alpha} + \Delta_{L,\alpha} - \sqrt{(\Delta_{\mathcal{X}_\alpha} + \Delta_{L,\alpha})^2 - \frac{\Delta_{\mathcal{X}_\alpha} \Delta_{L,\alpha}}{V}} \right). \quad (\text{B25})$$

This bound can be simplified by considering that $\Delta_{L,\alpha} = 1$. Then, in the thermodynamic limit $1/V \ll 1$, we get

$$\lambda_\alpha \geq \frac{\Delta_{\mathcal{X}_\alpha}}{4V(1 + \Delta_{\mathcal{X}_\alpha})}. \quad (\text{B26})$$

Replacing the latter inequality in Eq. B5 we finally obtain:

$$\Delta_\alpha \geq \frac{\Delta_{\mathcal{X}_\alpha}}{4V(1 + \Delta_{\mathcal{X}_\alpha})}. \quad (\text{B27})$$

Appendix C: Partition function as an observable

Here, we show how the total number of Hamiltonian cycles, that is, the infinite temperature partition function, is related to the expectation value of

$$\bigotimes_{\substack{2 \leq i \leq m \\ 2 \leq j \leq n}} \hat{P}_{ij}^x, \quad (\text{C1})$$

for a system in the state $|X_{\text{HC}}\rangle$.

Explicitly, the expectation value is

$$\begin{aligned} \langle X_{\text{HC}} | \bigotimes_{\substack{2 \leq i \leq m \\ 2 \leq j \leq n}} \hat{P}_{ij}^x | X_{\text{HC}} \rangle \\ = \frac{1}{|X_{\text{HC}}|} \sum_{\sigma, \sigma' \in X_{\text{HC}}} \langle \sigma' | \bigotimes_{\substack{2 \leq i \leq m \\ 2 \leq j \leq n}} \hat{P}_{ij}^x | \sigma \rangle. \end{aligned} \quad (\text{C2})$$

The computational basis states are tensor products of local configurations, i.e., $|\sigma\rangle = \bigotimes_{ij} |\sigma_{ij}\rangle$. Moreover, the plaquettes on the boundary of the dual lattice are fixed in the state $|\sigma_{ij}\rangle = |0\rangle$, so that $\langle \sigma'_{ij} | \sigma_{ij} \rangle = 1$ for all $(i, j) \notin [2, \dots, m-1] \times [2, \dots, n-1]$. Thus, the previous equation becomes

$$\begin{aligned}
& \langle X_{\text{HC}} | \bigotimes_{\substack{2 \leq i \leq m \\ 2 \leq j \leq n}} \hat{P}_{ij}^x | X_{\text{HC}} \rangle \\
&= \frac{1}{|X_{\text{HC}}|} \sum_{\sigma, \sigma' \in X_{\text{HC}}} \prod_{\substack{2 \leq i \leq m \\ 2 \leq j \leq n}} \langle \sigma'_{ij} | \hat{P}_{ij}^x | \sigma_{ij} \rangle \prod_{\substack{(i,j) \notin \\ [2, \dots, m-1] \times \\ [2, \dots, n-1]}} \langle 0 | 0 \rangle \\
&= \frac{1}{|X_{\text{HC}}|} \sum_{\sigma, \sigma' \in X_{\text{HC}}} \prod_{\substack{2 \leq i \leq m \\ 2 \leq j \leq n}} \frac{1}{2} \\
&= \frac{|X_{\text{HC}}|}{2^{(m-1)(n-1)}}, \tag{C3}
\end{aligned}$$

which allows us to infer the size $|X_{\text{HC}}|$ of the set of Hamiltonian cycles from the expectation value of $\bigotimes_{\substack{2 \leq i \leq m \\ 2 \leq j \leq n}} \hat{P}_{ij}^x$.

Appendix D: Convergence in bond dimension

In this appendix, we analyze the convergence of the various quality metrics and the entanglement of the MPS approximation discussed in the main text as a function of the bond dimension χ , as shown in Fig. 11.

In Panels (a–d), both the energy and the relative error in counting Hamiltonian cycles converge polynomially with the bond dimension, with the convergence rate decreasing as the system size increases. For square lattices, convergence only begins once the bond dimension exceeds a threshold value that grows rapidly with system size, preventing an efficient approximation.

This behaviour is clarified by examining the maximum bipartition entanglement entropy in Panels (e) and (f). For rectangular lattices, a bond dimension of about $\chi \gtrsim 64$ already suffices to capture the relevant correlations. In contrast, for square lattices, the bond dimension required for entanglement convergence increases sharply with system size. Before convergence is reached, the entanglement is underestimated because the MPS truncation discards part of the Schmidt spectrum.

As anticipated in the main text, these observations are consistent with an area-law entanglement scaling.

Appendix E: Quadratic speedup in counting

Here, we show that quantum amplitude amplification [23, 55] quadratically speeds up the count of Hamiltonian cycles with respect to Monte Carlo sampling, provided a unitary algorithm

$$\hat{\mathcal{A}}|0 \dots 0\rangle = |X_{\text{HC}}\rangle \tag{E1}$$

that prepares the coherent quantum sample $|X_{\text{HC}}\rangle$. The algorithm $\hat{\mathcal{A}}$ could be, for example, a quantum annealing schedule ending with the Hamiltonian \hat{H}_{HC} .

Equation 30 allows us to estimate the ratio r between the total number of Hamiltonian cycles and the dimension of the lattice configuration space by measuring the expectation value of $\bigotimes_{\substack{2 \leq i \leq m \\ 2 \leq j \leq n}} \hat{P}_{ij}^x$ for the state $|X_{\text{HC}}\rangle$. Let

\hat{H} be the Hadamard gate. Since

$$\hat{P}^x = \hat{H}\hat{P}^+\hat{H} = \hat{H}|1\rangle\langle 1|\hat{H}, \tag{E2}$$

we can write

$$\begin{aligned}
r &= \langle X_{\text{HC}} | \bigotimes_{\substack{2 \leq i \leq m \\ 2 \leq j \leq n}} \hat{P}_{ij}^x | X_{\text{HC}} \rangle \\
&= \langle X_{\text{HC}} | \hat{H}^{\otimes n \cdot m} \left(\bigotimes_{\substack{2 \leq i \leq m \\ 2 \leq j \leq n}} |1\rangle\langle 1|_{ij} \right) \hat{H}^{\otimes n \cdot m} | X_{\text{HC}} \rangle \\
&= \left| \langle 1 \dots 1 | \left(\hat{H}^{\otimes n \cdot m} | X_{\text{HC}} \rangle \right) \right|^2 \\
&= \left| \langle 1 \dots 1 | \left(\hat{H}^{\otimes n \cdot m} \hat{\mathcal{A}} | 0 \dots 0 \rangle \right) \right|^2. \tag{E3}
\end{aligned}$$

Thus, r is the probability of sampling the state $|1 \dots 1\rangle$ when the system is in the state $\hat{H}^{\otimes n \cdot m} | X_{\text{HC}} \rangle$:

As anticipated in the main text, this probability is exponentially small in the lattice size. As a consequence, estimating r up to a fixed acceptable relative error requires an exponential number of samples $N_S = \mathcal{O}(1/r)$. Despite this, Monte Carlo estimation remains a valid approach when considering squared lattices, where the state-of-art transfer-matrix counting methods also exhibit exponential cost. It is therefore meaningful to employ amplitude amplification to boost the estimation of r .

We apply amplitude amplification as follows. First, we prepare the system in the state $\hat{H}^{\otimes n \cdot m} | X_{\text{HC}} \rangle$. Then, we repeatedly apply the operator

$$\hat{W} = \hat{S}_{\text{HC}} \hat{S}_1, \tag{E4}$$

where

$$\hat{S}_1 = \mathbb{1} - 2|1 \dots 1\rangle\langle 1 \dots 1| \tag{E5}$$

reflects the system state with respect to the state $|1 \dots 1\rangle$, and

$$\hat{S}_{\text{HC}} = \left(\mathbb{1} - 2\hat{H}^{\otimes n \cdot m} | X_{\text{HC}} \rangle \langle X_{\text{HC}} | \hat{H}^{\otimes n \cdot m} \right), \tag{E6}$$

reflects the system state with respect to $\hat{H}^{\otimes n \cdot m} | X_{\text{HC}} \rangle$. We note that the knowledge of $\hat{\mathcal{A}}$ provides a recipe for implementing \hat{S}_{HC} . Indeed, we can write

$$\begin{aligned}
\hat{S}_{\text{HC}} &= \hat{H}^{\otimes n \cdot m} \hat{\mathcal{A}} (\mathbb{1} - 2|0 \dots 0\rangle\langle 0 \dots 0|) \hat{\mathcal{A}}^\dagger \hat{H}^{\otimes n \cdot m} \\
&= \hat{H}^{\otimes n \cdot m} \hat{\mathcal{A}} \hat{X}^{\otimes n \cdot m} \hat{S}_1 \hat{X}^{\otimes n \cdot m} \hat{\mathcal{A}}^\dagger \hat{H}^{\otimes n \cdot m}, \tag{E7}
\end{aligned}$$

where \hat{X} is a spin-flip gate. Finally, the operator \hat{S}_1 can be implemented efficiently on a quantum computer as a multi-controlled NOT gate.

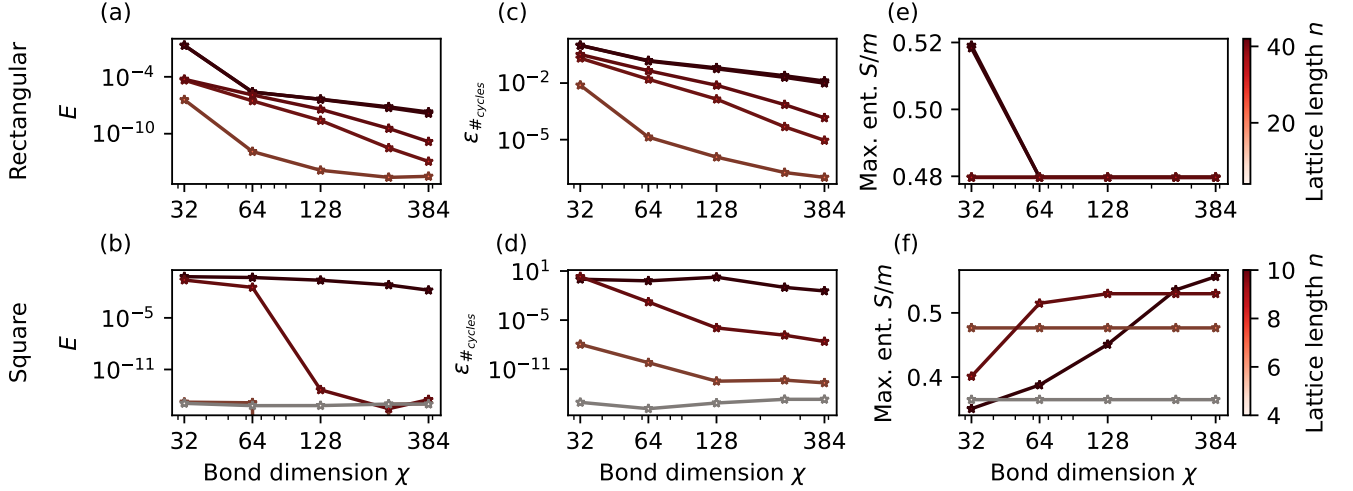


FIG. 11. Convergence of the MPS approximation of $|X_{\text{HC}}\rangle$ as a function of the bond dimension χ . Panels (a,c,e) correspond to rectangular lattices of size $6 \times n$, while Panels (b,d,f) correspond to square lattices of size $n \times n$. **Panels (a,b):** Tensor-network energy E . **Panels (c,d):** Relative error in the number of Hamiltonian cycles. **Panels (e,f):** Maximum bipartition entanglement entropy, normalized by the boundary area.

After $\mathcal{O}(1/\sqrt{r})$ applications of the operator \hat{W} , the probability $p_{1\dots 1}$ of measuring $|1\dots 1\rangle$ approaches unity [23, 55]. The number of samples needed to verify that $p_{1\dots 1} \approx 1$ does not depend on the specific starting

state. Consequently, $N_C = \mathcal{O}(1/\sqrt{r})$ calls to \hat{A} are required to estimate r with fixed relative accuracy, yielding a quadratic reduction compared to the $\mathcal{O}(1/r)$ samples needed by classical Monte Carlo methods.

-
- [1] Carlo Vanderzande, *Lattice Models of Polymers*, Cambridge Lecture Notes in Physics (Cambridge University Press, 1998).
- [2] J. F. Nagle, “Statistical mechanics of the melting transition in lattice models of polymers,” *Proceedings of the Royal Society of London. A. Mathematical and Physical Sciences* **337**, 569–589 (1974).
- [3] M Gorodn, P Kapadia, and A Malakis, “The graph-like state of matter. vii. the glass transition of polymers and hamiltonian walks,” *Journal of Physics A: Mathematical and General* **9**, 751 (1976).
- [4] Rhonald Lua, Alexander L. Borovinskiy, and Alexander Yu. Grosberg, “Fractal and statistical properties of large compact polymers: a computational study,” *Polymer* **45**, 717–731 (2004), conformational Protein Conformations.
- [5] Angelo Rosa and Ralf Everaers, “Ring polymers in the melt state: The physics of crumpling,” *Phys. Rev. Lett.* **112**, 118302 (2014).
- [6] Jesper Lykke Jacobsen, “Unbiased sampling of globular lattice proteins in three dimensions,” *Phys. Rev. Lett.* **100**, 118102 (2008).
- [7] E.C. Dykeman, N.E. Grayson, K. Toropova, N.A. Ranson, P.G. Stockley, and R. Twarock, “Simple rules for efficient assembly predict the layout of a packaged viral rna,” *Journal of Molecular Biology* **408**, 399–407 (2011).
- [8] Reidun Twarock, German Leonov, and Peter G. Stockley, “Hamiltonian path analysis of viral genomes,” *Nature Communications* **9**, 2021 (2018).
- [9] Reidun Twarock, Richard J Bingham, Eric C Dykeman, and Peter G Stockley, “A modelling paradigm for rna virus assembly,” *Current Opinion in Virology* **31**, 74–81 (2018), virus structure and expression • Viral evolution.
- [10] R. Ramakrishnan, J. F. Pekny, and J. M. Caruthers, “A combinatorial algorithm for effective generation of long maximally compact lattice chains,” *The Journal of Chemical Physics* **103**, 7592–7604 (1995).
- [11] Mattia Alberto Ubertaini and Angelo Rosa, “Computer simulations of melts of ring polymers with nonconserved topology: A dynamic monte carlo lattice model,” *Phys. Rev. E* **104**, 054503 (2021).
- [12] Marc L. Mansfield, “Unbiased sampling of lattice hamilton path ensembles,” *The Journal of Chemical Physics* **125**, 154103 (2006).
- [13] Robert Stoyan and Volker Strehl, “Enumeration of hamiltonian circuits in rectangular grids,” *Journal of Combinatorial Mathematics and Combinatorial Computing* **21**, 109–128 (1996).
- [14] Jesper Lykke Jacobsen, “Exact enumeration of hamiltonian circuits, walks and chains in two and three dimensions,” *Journal of Physics A: Mathematical and Theoretical* **40**, 14667–14678 (2007).
- [15] Cristian Micheletti, Philipp Hauke, and Pietro Faccioli, “Polymer physics by quantum computing,” *Phys. Rev. Lett.* **127**, 080501 (2021).
- [16] Francesco Slongo, Philipp Hauke, Pietro Faccioli, and Cristian Micheletti, “Quantum-inspired encoding enhances stochastic sampling of soft matter systems,” *Sci-*

- ence *Advances* **9** (2023).
- [17] Veronica Panizza, Alessandro Roggero, Philipp Hauke, and Pietro Faccioli, “Statistical mechanics of heteropolymers from lattice gauge theory,” *Phys. Rev. Lett.* **134**, 158101 (2025).
- [18] Tadashi Kadowaki and Hidetoshi Nishimori, “Quantum annealing in the transverse Ising model,” *Physical Review E* **58**, 5355–5363 (1998).
- [19] Edward Farhi, Jeffrey Goldstone, Sam Gutmann, Joshua Lapan, Andrew Lundgren, and Daniel Preda, “A quantum adiabatic evolution algorithm applied to random instances of an NP-complete problem,” *Science* **292**, 472–475 (2001).
- [20] Giuseppe E. Santoro, Roman Martonak, Erio Tosatti, and Roberto Car, “Theory of quantum annealing of an Ising spin glass,” *Science* **295**, 2427–2430 (2002).
- [21] Tameem Albash and Daniel A. Lidar, “Adiabatic quantum computation,” *Reviews of Modern Physics* **90**, 015002 (2018).
- [22] Leonid Libkin, *Elements of finite model theory* (Springer, Berlin, 2004).
- [23] G. Brassard and P. Hoyer, “An exact quantum polynomial-time algorithm for simon’s problem,” in *Proceedings of the Fifth Israeli Symposium on Theory of Computing and Systems*, ISTCS-97 (IEEE Comput. Soc) p. 12–23.
- [24] Ashley Montanaro, “Quantum speedup of monte carlo methods,” *Proceedings of the Royal Society A: Mathematical, Physical and Engineering Sciences* **471**, 20150301 (2015).
- [25] Davide Rattacaso, Daniel Jaschke, Marco Ballarín, Ilaria Siloi, and Simone Montangero, “Quantum algorithms for equational reasoning,” (2025), arXiv:2508.21122 [quant-ph].
- [26] J Werschnik and E K U Gross, “Quantum optimal control theory,” *J. Phys. B: At. Mol. Opt. Phys.* **40**, R175–R211 (2007).
- [27] Patrick Doria, Tommaso Calarco, and Simone Montangero, “Optimal control technique for many-body quantum dynamics,” *Physical Review Letters* **106**, 190501 (2011).
- [28] Tommaso Caneva, Tommaso Calarco, and Simone Montangero, “Chopped random-basis quantum optimization,” *Phys. Rev. A* **84**, 022326 (2011).
- [29] Edward Farhi, Jeffrey Goldstone, and Sam Gutmann, “A quantum approximate optimization algorithm,” (2014), arXiv preprint, arXiv:1411.4028 [quant-ph].
- [30] Edward Farhi and Aram W Harrow, “Quantum supremacy through the quantum approximate optimization algorithm,” (2019), arXiv preprint, arXiv:1602.07674 [quant-ph].
- [31] Kostas Blekos, Dean Brand, Andrea Ceschini, Chiao-Hui Chou, Rui-Hao Li, Komal Pandya, and Alessandro Summer, “A review on quantum approximate optimization algorithm and its variants,” *Physics Reports* **1068**, 1–66 (2024).
- [32] Sam McArdle, Tyson Jones, Suguru Endo, Ying Li, Simon C. Benjamin, and Xiao Yuan, “Variational ansatz-based quantum simulation of imaginary time evolution,” *npj Quantum Information* **5** (2019).
- [33] Mario Motta, Chong Sun, Adrian T. K. Tan, Matthew J. O’Rourke, Erika Ye, Austin J. Minnich, Fernando G. S. L. Brandão, and Garnet Kin-Lic Chan, “Determining eigenstates and thermal states on a quantum computer using quantum imaginary time evolution,” *Nature Physics* **16**, 205–210 (2020).
- [34] Hirsh Kamakari, Shi-Ning Sun, Mario Motta, and Austin J. Minnich, “Digital quantum simulation of open quantum systems using quantum imaginary-time evolution,” *PRX Quantum* **3**, 010320 (2022).
- [35] Marek Gluza, Jeongrak Son, Bi Hong Tiang, René Zander, Raphael Seidel, Yudai Suzuki, Zoë Holmes, and Nelly H. Y. Ng, “Double-bracket quantum algorithms for quantum imaginary-time evolution,” (2025), arXiv:2412.04554 [quant-ph].
- [36] Zhiyan Ding, Yongtao Zhan, John Preskill, and Lin Lin, “End-to-end efficient quantum thermal and ground state preparation made simple,” (2025), arXiv:2508.05703 [quant-ph].
- [37] U. Schollwöck, “The density-matrix renormalization group,” *Rev. Mod. Phys.* **77**, 259–315 (2005).
- [38] Simone Montangero, *Introduction to Tensor Network Methods* (Springer, 2018).
- [39] Camille Jordan, *Cours d’analyse de l’École polytechnique*, Vol. 1 (Gauthier-Villars et fils, 1893).
- [40] Frank Harary, *Graph theory (on Demand Printing of 02787)* (CRC Press, 2018).
- [41] Rahnema Islam Nishat and Sue Whitesides, “Bend complexity and hamiltonian cycles in grid graphs,” in *Computing and Combinatorics*, edited by Yixin Cao and Jianer Chen (Springer International Publishing, Cham, 2017) pp. 445–456.
- [42] Rahnema Islam Nishat and Sue Whitesides, “Reconfiguring hamiltonian cycles in l-shaped grid graphs,” in *Graph-Theoretic Concepts in Computer Science*, edited by Ignasi Sau and Dimitrios M. Thilikos (Springer International Publishing, Cham, 2019) pp. 325–337.
- [43] Rahnema Islam Nishat, *Reconfiguration of Hamiltonian cycles and paths in grid graphs*, Ph.D. thesis (2020).
- [44] Andrew Y. Ng, Michael I. Jordan, and Yair Weiss, “On spectral clustering: analysis and an algorithm,” in *Proceedings of the 15th International Conference on Neural Information Processing Systems: Natural and Synthetic*, NIPS’01 (MIT Press, Cambridge, MA, USA, 2001) p. 849–856.
- [45] Ulrike von Luxburg, “A tutorial on spectral clustering,” *Statistics and Computing* **17**, 395–416 (2007).
- [46] Ravi Montenegro and Prasad Tetali, “Mathematical aspects of mixing times in markov chains,” *Foundations and Trends® in Theoretical Computer Science* **1**, 237–354 (2006).
- [47] Paul R Halmos, “Two subspaces,” *Transactions of the American Mathematical Society* **144**, 381–389 (1969).
- [48] A. Böttcher and I.M. Spitkovsky, “A gentle guide to the basics of two projections theory,” *Linear Algebra and its Applications* **432**, 1412–1459 (2010).
- [49] Jutho Haegeman, Christian Lubich, Ivan Oseledets, Bart Vandereycken, and Frank Verstraete, “Unifying time evolution and optimization with matrix product states,” *Phys. Rev. B* **94**, 165116 (2016).
- [50] Ulrich Schollwöck, “The density-matrix renormalization group in the age of matrix product states,” *Annals of Physics* **326**, 96–192 (2011), january 2011 Special Issue.
- [51] Pietro Silvi, Ferdinand Tschirsich, Matthias Gerster, Johannes Jünemann, Daniel Jaschke, Matteo Rizzi, and Simone Montangero, “The tensor networks anthology: Simulation techniques for many-body quantum lattice

- systems,” *SciPost Phys. Lect. Notes*, **8** (2019).
- [52] Giovanni Cataldi, Ashkan Abedi, Giuseppe Magnifico, Simone Notarnicola, Nicola Dalla Pozza, Vittorio Giovannetti, and Simone Montangero, “Hilbert curve vs hilbert space: exploiting fractal 2d covering to increase tensor network efficiency,” *Quantum* **5**, 556 (2021).
- [53] Flavio Baccari, Davide Bacilieri, Marco Ballarin, Francesco Pio Barone, Francesco Campaioli, Alberto Giuseppe Catalano, Giovanni Cataldi, Alberto Coppi, Aurora Costantini, Asmita Datta, Andrea De Girolamo, Daniel Jaschke, Sven Benjamin Kožić, Giuseppe Magnifico, Carmelo Mordini, Simone Montangero, Simone Notarnicola, Alice Pagano, Luka Pavesic, Davide Rattacaso, Marco Rigobello, Nora Reinić, Simone Scarlatella, Ilaria Siloi, Pietro Silvi, Marco Tesoro, Gianpaolo Torre, and Darwin Wanisch, “Quantum tea: qtealeaves,” (2025).
- [54] Marco Ballarin, Pietro Silvi, Simone Montangero, and Daniel Jaschke, “Optimal sampling of tensor networks targeting wave function’s fast decaying tails,” *Quantum* **9**, 1714 (2025).
- [55] Lov K. Grover, “Quantum computers can search rapidly by using almost any transformation,” *Physical Review Letters* **80**, 4329–4332 (1998).
- [56] Veronica Panizza, Philipp Hauke, Cristian Micheletti, and Pietro Faccioli, “Protein design by integrating machine learning and quantum-encoded optimization,” *PRX Life* **2**, 043012 (2024).
- [57] Salvador Elías Venegas-Andraca, “Quantum walks: a comprehensive review,” *Quantum Information Processing* **11**, 1015–1106 (2012).